

**Design and Construction of a Positron Emission Tomography
(PET) Unit and Medical Applications with
GEANT Detector Simulation Package**

Sayın Hocam'a
Hürmetlerimle...
Müge Karagöz

by

Müge Karagöz

B.S. in Physics, Boğaziçi University, 1996

Submitted to the Institute for Graduate Studies in
Science and Engineering in partial fulfillment of
the requirements for the degree of
Master of Science
in
Physics

Boğaziçi University

1998

Acknowledgments

I would like to thank to Prof. Dr. Engin Arik for giving me the possibility to participate in the activities of the H.E.P. laboratory at Bogazici University and to write this thesis. I am grateful to Prof. Dr. Metin Arik and Turkish Balkan Center for Physics Research and Applications who provided the financial support for the scintillation crystals. I also would like to thank to Prof. Dr. Muzaffer Ata for donating the position sensitive PMT.

I would like to express my very deep gratitude to Dr. Arif Mailov for all he did and all he taught. Without his support, this work would have never ended. He is the “arif”.

I am thankful to mer İlday and Bahadır zus for proofreading and for their encouragements and to Tolga “Thorr” Orhon for his help on “construction”. I would like also to thank to all group members for their invaluable support.

I would like to thank my family for their never-ending support, understanding and love.

I finally thank my NGU, Dr. N. Gkhan nel, for *himself*. It is his belief in me that gives me the power.

Abstract

In order to investigate the possibility of the construction of a sample PET coincidence unit in our HEP laboratory, a setup with two face to face PMTs and two 2x8 CsI(Tl) scintillator matrices has been constructed. In this setup, 1-D projections of a pointlike ^{22}Na positron source at different angles have been measured. Using these projections a 2-D image has been formed. Monte Carlo studies of this setup have been implemented using the detector simulation tool in CERN program library, GEANT. Again with GEANT a sample human body is created to study the effects of proton therapy. Utilization of the simulation as a pretherapy tool is also investigated.

Özet

YEF laboratuvarımızda bir örnek PET ünitesinin yapım imkanını araştırmak için, yüz yüze bakan iki PMT ve iki 2x8 CsI(Tl) sintilatör matrisinden oluşan bir düzenek kuruldu. Bu düzenekte noktasal ^{22}Na pozitron kaynağının değişik açılardan alınmış 1 boyutlu izdüşümleri ölçüldü. Bu izdüşümler kullanılarak 2 boyutlu görüntü oluşturuldu. Bu düzenegin Monte Carlo çalışmaları CERN program kütüphanesindeki GEANT dedektör simülasyon paketi ile yapıldı. Yine GEANT ile proton terapisinin etkilerini incelemek için örnek bir insan vücudu yaratıldı. Terapi öncesi uygulama olarak simülasyonun kullanılması da araştırıldı.

Contents

Acknowledgments	ii
Abstract	iii
Özet	iv
Table of Contents	vi
List of Figures	viii
List of Tables	ix
List of Symbols	x
1 INTRODUCTION	1
2 MEDICAL IMAGING	3
2.1. Different Techniques in Medical Imaging and Tomography	3
2.2. Overview of PET	5
3 PET THEORY	10
3.1. Physics Behind PET - Particle Interactions	10
3.1.1. Particle Interactions with Matter	10
3.1.2. Electron-Positron Interactions with Matter	10
3.1.3. Photon Interactions with Matter	14
3.2. Scintillation and Scintillators	20
3.2.1. Comparing Organic and Inorganic Scintillators	20
3.2.2. A Type of Inorganic Scintillator: CsI(Tl)	22
3.3. PET requirements	24
3.3.1. PET Detector Requirements	24
3.3.2. PET Scintillator Requirements	25

4	OVERVIEW OF GEANT, A MONTE CARLO SIMULATION PACKAGE	27
4.1.	Geometry and Physical Parameters	28
4.2.	GEANT Particles and Processes	29
4.3.	Flowchart and Tracking Process	30
5	SIMULATION OF THE PET UNIT	33
5.1.	Setup Description	33
5.2.	Simulations and Analysis	35
6	DATA TAKING AND ANALYSIS	40
6.1.	General Description	40
6.2.	Test of the PSPMT and Crosstalk Measurement	41
6.2.1.	Analysis	44
6.3.	PET Unit Measurements	51
6.3.1.	Gamma Ray Spectroscopy with CsI(Tl) Crystals	51
6.3.2.	Measurements with PET Unit and Image Reconstruction	56
7	CONCLUSION	62
	Appendix A	63
	Appendix B	70
	Appendix C	71
	Appendix D	72
	Appendix E	73
	REFERENCES	88

List of Figures

2.1	Illustrative Description of Positron-Electron Annihilation	7
2.2	PET System	8
2.3	The Line of Response for two Detectors in Coincidence [12]	9
3.1	Lowest Order Feynman Diagrams for Bremsstrahlung	12
3.2	Feynman Diagram for e^+e^- Annihilation	13
3.3	Photoelectric Effect: Photon in - Electron out!	16
3.4	Compton Scattering	17
3.5	Feynman Diagram for Compton Scattering	18
3.6	Lowest Order Feynman Diagrams for Pair Production.	19
3.7	Cross Section Plots for CsI	23
3.8	Cross Section Plots for Polystyrene	23
4.1	Over-simplified GEANT Flowchart	30
5.1	Geometric Tree Structure of the System Simulated with GEANT	34
5.2	Scintillator Block as Specified in GEANT	34
5.3	A Perspective View of the System Simulated with GEANT	36
5.4	Electron Energy Distribution	36
5.5	Cross Sectional View of UNIT and Crosstalk at Gamma Interaction Level	37
5.6	Results for $x=0.9$ cm	38
6.1	Signal Shape	42
6.2	Setup for the Crosstalk Measurement	42
6.3	General View of the Surface Scan Setup	43
6.4	A Typical Cluster Length, COG and PH Distributions in Y Direction .	46

6.5	COGX vs COGY Graphs Simultaneously Plotted for all Scan Points . .	47
6.6	COGX vs COGY Values Plotted at the Wire Cross Points	48
6.7	COG Plots In X Direction For Point 38	50
6.8	The DAQ of the Spectroscopy Measurement	52
6.9	Pulse Height Spectra for Different Sources and Scintillators	52
6.10	Preamplifier for Enhancing the Resolution of the Energy Peaks	54
6.11	Pulse Height Spectra After the Preamplifier	55
6.12	Schematic View of the PET Coincidence System Setup	57
6.13	Rotation Directions for Data-taking	58
6.14	The DAQ Setup of the Coincidence Measurement	59
6.15	COG Plots for Different Detector Angles	60
6.16	3-D and 2-D Representations of the Reconstructed Image	61
7.1	Comparison of Different Radiation Types Currently Used in Radiation Therapy [51]	64
7.2	Human Body Viewed from the Projection on X-Z Plane.	65
7.3	Bragg Peak Curve and Spread of Protons from Initial Direction for 100 MeV Protons	67
7.4	Graph Showing the Dependence of Proton Energy to Range in Soft Tis- sue. Curve is fitted to equation 7.2	68
7.5	Equivalent circuit of the detector-amplifier system	72

List of Tables

2.1	Positron Sources Commonly Used in PET	6
2.2	Some Applications of Positron Emitters	6
3.1	Comparison Table for Scintillators	26
6.1	Results of Crosstalk Measurements	49
6.2	Results of Gaussian Fits and Energy Resolutions	56
7.1	Table of Obtained Values for Different Proton Energies	69

List of Symbols

dE/dx : stopping power, specific energy loss

Z : atomic number

σ : interaction cross section

T : kinetic energy

X_{COG}, Y_{COG} : center of gravities of a cluster

PH : pulse height

FWHM: full width at half maximum

R : resolution in per cent

θ : projection angle

$P(COG, \theta)$: projection matrix

f_{back} : backprojection matrix

M : number of projection angles

d_{soft} : density of soft tissue

d_{bone} : density of bone tissue

T_p : kinetic energy of the proton

R_{spread} : radial spread of protons

1. INTRODUCTION

Starting from the development of simple particle accelerators, the experimental high energy physicists have been devising new techniques to reach higher energies in order to find new particles, thus to explore new phenomena. The requirements to accomplish this task came together with the requirements of fast detectors and efficient readout systems which made High Energy Physics (HEP) the driving force for technological development.

The advances in HEP or particle physics in general, have also largely contributed to the domain of medical sciences [1]. One can count radionuclide imaging and radiotherapy as examples to such a contribution. Radionuclide imaging is now a popular topic in particle physics research centers such as CERN. Similarly, the construction of compact accelerators permitted the spreading of radiation therapy centers. The interdisciplinary research in particle physics and medicine makes a very interesting and fruitful collaboration. For any physicist, to observe the outcomes of his research to be applied to the human health is very fascinating.

We wanted to take part in the medical applications of experimental particle physics. To take the first steps through this goal, we decided to investigate the possibility of the construction of a sample Positron Emission Tomography (PET) coincidence unit with data acquisition systems used in HEP. The second chapter of this work is devoted to an overview of medical imaging techniques and PET. In the third chapter, we outlined the physics behind PET in order to understand the interactions that lead to detection characteristics of particles and the requirements for a PET camera. Before performing any experiment it is always useful to simulate it. In chapter four, we briefly described the detector simulation package, GEANT, of the CERN program library. We used this tool to simulate our coincidence setup and to investigate the detection characteristics of gamma rays with CsI crystals. We report about the results of this simulation in chapter five. Before performing the real coincidence and source imaging experiments, we wanted to test out position sensitive photomultiplier tube (PSPMT) and CsI(Tl)

crystals separately. In chapter six, we first explained about the crosstalk measurements which has the objective of testing the PSPMT and finding the crosstalk of our full system including the data acquisition part. In order to understand the energy response of our crystals we performed pulse height measurements with different γ sources and we compared the CsI(Tl) crystals with organic plastic scintillators. Finally, we have constructed a coincidence setup with two face-to-face photomultiplier tubes each coupled to a 2x8 matrix array of CsI(Tl) crystals. Rotating the pointlike ^{22}Na source permitted us to obtain its 1-D projections from different viewing angles and to test the basics of 2-D image reconstruction.

A software investigation of another medical topic, namely proton therapy, was described in Appendix A. We implemented a detector geometry that represented the human body in GEANT detector simulation package and investigated the possibility of deciding the proton beam energy according to the localization of any tumor within this body. We report about the results of this simulation which lead to a curve yielding this dependence.

2. MEDICAL IMAGING

2.1. Different Techniques in Medical Imaging and Tomography

Medical imaging is a powerful clinical diagnostic tool used in modern medicine. Starting from the discovery of X-rays in 1895 by Roentgen, the use of different techniques has been investigated and the field of medical imaging is now growing at a speed that has never been reached before. X-ray is the most commonly used modality among the recently improving ones which can be classified as radionuclide imaging, ultrasound and magnetic resonance imaging. These three are widely accepted since the second half of the century and all of these modalities are advantageous from one another by their applicability and reliability for different types of clinical diagnoses.

X-ray is the favorite method for imaging bone and lung tissue and investigations concerning the tissue density. Conventional X-ray radiography, the method public is most familiar with, utilizes the attenuation of X-rays in specific tissues of the body and yields a 2-D image formed on a film or on screen. Sometimes a contrast material can be injected to the patient as in the case of mammography (radiographic examination of the breast) or the image can be visualized directly on a fluorescent screen as in fluoroscopy. For further enhancements in image quality and to compensate for the limitations on depth localization caused by projecting a 3-D structure on a 2-D picture, the method of tomographical imaging is applied to X-ray radiography [2]. Tomography¹ is a depth-discrimination technique which produces “images of objects within the human body in which structures at a chosen depth are clearly shown, whereas those at other depths are either blurred, absent, or identified as to depth” [3].

Ultrasound is convenient especially when no radiation exposure is desired since this method necessitates no electromagnetic radiation but simply relies on acoustic prin-

¹the Greek word *temnein* means to cut

ciples for ultrasound waves with frequencies above the upper limit of human audible range (> 20 kHz). This modality is used for physiological investigation purposes and for imaging parts of the body that are in motion such as heart valves [2].

Nuclear magnetic resonance imaging (NMRI) is another modality clinically utilized for physiological diagnosis. NMRI has its basis on the phenomenon of nuclear magnetic resonance which utilizes electromagnetic radiation to investigate the fundamental properties of matter. The basic principle behind this method is the observation of the quantum mechanically expected consequences of the interaction of radiation with the nuclear magnetic moment. This radiation is in the radio frequency (RF) range of the electromagnetic spectrum. The method operates with non-ionizing radiation and is preferred for its good resolution. One advantageous property of NMRI is that these waves are able to penetrate skeletal and air filled structures with negligible attenuation, thus it is suitable for producing anatomical images. In principle, the body is immersed in a static magnetic field in order to align the nuclear spins and it is also subjected to an alternating RF magnetic field. In this way, the orientations of the nuclear spins relative to the direction of the static field are changed alternately. These changes cause the nuclei to absorb energy and emit the same energy when the RF field is turned off. The detection of this emission makes it possible to get an image of the part of the body under investigation [2, 5].

The last type of imaging modality that we will mention is radionuclide imaging. Radionuclide is a term that describes a nucleus with a measurable certain half-life of radioactive decay. The use of radionuclides for diagnostic purposes in medicine was first started by Hevesy in 1935 [2]. The advance in instrumentation was the introduction of the scintillation camera, generally known as the "Anger Camera", to the field by Anger in 1957 [4]. Later on, in 1963, it was shown by Kuhl and Edwards that radiographic tomography methods could be applied to radionuclide imaging [3]. Radionuclide imaging yields detailed information about the physiological or metabolic functioning of the tissues by making use of radioactive isotopes. Two recent and popular methods for this type of diagnosis are

- Single-photon emission computed tomography (SPECT),
- Positron emission tomography [6]-[11].

The latter is the most important to this work and will be described in detail in the next section.

SPECT has similar basics to that of X-ray CT. As in X-ray CT, it involves the rotation of a detector array around the body. The main difference is that in X-ray CT, the attenuation of the known radiation (in the range 20-120 keV) is measured, whereas in SPECT single photons (of usually about 140 keV) that emerge from the radionuclide (usually technetium-99m) that is concentrated in the patient's body are detected and measured. This method of imaging is in great improvement and is becoming more attractive following the rapid development of new radiopharmaceuticals and image processing techniques. However, the efficiency problem pertains due to the collimators used to identify the energy and the direction of each photon individually.

2.2. Overview of PET

The history of PET, a radionuclide imaging technique, can be traced back to early 1950's. In 1951, positron emitters were suggested as potential substances to be used in medical imaging, but they were not in use until 1960's. PET allows *in vivo*² measurements of physiological and metabolic functions and processes such as brain activation which is impossible to measure otherwise. The advantage of the positron emitting radionuclides is that they are the radioisotopes of the most common elements in the human body (i.e., ^{11}C , ^{13}N , ^{15}O). Thus, these materials can be safely used to label organic molecules without leaving any artifacts which may modify the metabolism. The drawback of using positron emitters is that they are generally very short-lived radioisotopes so they have to be produced in a cyclotron nearby.

Some typical properties of positron sources is given in table 2.1 [12]. The energy of the positron is related to the distance it traverses within the body and it is also im-

²alive

portant for the ionisation effect in the body. One can see that even the longest living radionuclide has an half life of about 110 minutes. The last two parameters listed in the table is mainly important for detection purposes, especially for the localization of a tumor.

Table 2.1: Positron Sources Commonly Used in PET

	^{18}F	^{11}C	^{13}N	^{15}O	^{68}Ga
Maximum β^+ Energy (Mev)	0.633	0.959	1.197	1.378	1.898
Most Probable β^+ Energy (Mev)	0.202	0.326	0.432	0.696	0.783
Half Life (min)	109.8	20.4	9.96	2.07	68.3
Max Path Length in Water (mm)	2.4	5.0	5.4	8.2	9.1
Radial Range in Water (FWHM mm)	1.0	1.1	1.4	1.5	1.7

Table 2.2: Some Applications of Positron Emitters

	radionuclide	tracer
Glucose metabolic rate	^{18}F	flourodeoxyglucose
Whole body oncology	^{18}F	flourodeoxyglucose
Regional blood flow and blood volume	^{13}N	ammonia
Cerebral oxygen metabolic rate	^{15}O	water
Amino acid metabolism	^{11}C	methionine
Neurology (Parkinson's disease)	^{18}F	flourodopa

The imaging with PET also requires a substance called the tracer which is a biological molecule that carries with it a positron-emitter to be introduced into the patient's body. Without a tracer, the radionuclide cannot be injected to the body. It's desired that the proper tracer should be used for different diagnostic purposes since each tracer accommodates itself within several minutes in the specific tissue for which it has an affinity. For example an ^{18}F labelled glucose tracer (fluorodeoxyglucose) is used to investigate the brain since glucose is the primary source of energy for the brain. Thus,

in nuclear medicine, an appropriate tracer is chosen for part of the body which is under investigation. Table 2.2. lists some of the medical applications of radioisotopes used in PET [5].

PET has many benefits compared to other imaging methodologies. Probably the most important one is that PET provides a direct measurement of metabolic activity and information about the physiology of the body which plays a crucial role in diagnosis. PET can reduce costs in the diagnosis and treatment of many significant diseases in oncology, neurology and cardiology. Especially in cancer diagnosis, the differentiation between a malignant and a benign lesion³ can be easily made. Thus, it eliminates or reduces unnecessary surgeries or treatments. This differentiation is due to the higher glucose consumption of cancer cells than neighboring healthy cells. It also helps saving time because of the fact that it can be used to scan all parts of the body in one single examination. A benefit, important from the point of view of radiation health, is that PET does not leave any artifacts and radioactive substances since only short-lived isotopes of the chemical substances known to the body are introduced to the patient. Besides all these advantages, PET, compared to its nearest relative SPECT, is much more sensitive (electronic collimation [2]) and has a higher resolution in image reconstruction.

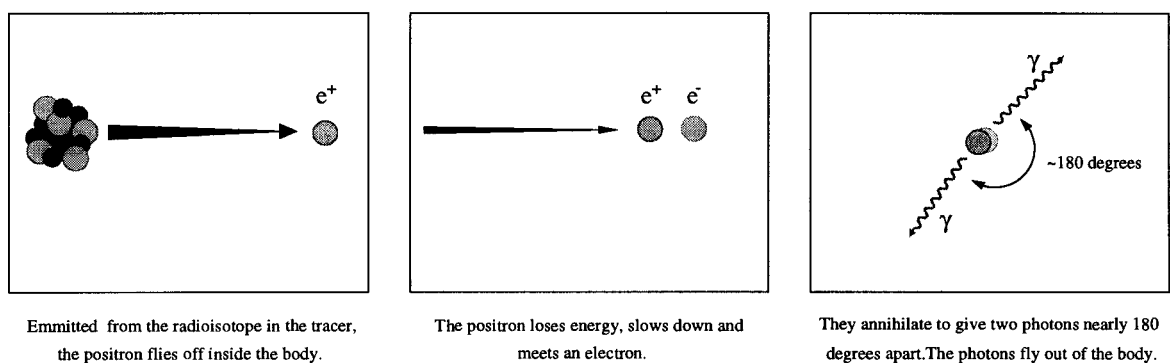


Figure 2.1: Illustrative Description of Positron-Electron Annihilation

The PET system mainly consists of an array of detectors similar to the structure

³A structural or biochemical change in an organ or tissue produced by disease processes or a wound.

of X-ray CT and SPECT systems as is illustrated in figure 2.2. A circular array of detector units form a ring, the diameter of which defines the plane of detection (field of view), around the patient. Detector units are operated to detect 511 keV gammas that are emitted from the specific region of the patient's body where the radiotracer has been concentrated in. The gammas are emitted due to the fact that the positron emitted from the tracer annihilates with an electron within a short time. Each detector is made, then, potentially in coincidence with another unit on the opposite side of the ring, that is, when back-to-back gammas are emitted, both are expected to give signals within some time window. The line (chord) joining these coincident detectors, then, informs that the positron annihilation has occurred somewhere in between these detectors (fig. 2.3). Using this information acquired from each opposite units, a 2-D slice image (tomograph) can be obtained within the plane defined by the ring. If 3-D images are required to be formed, then several rings can be used on top of each other forming stacks [13]. Most modern PET cameras consist of such a geometry. There are also some other PET systems such as time-of-flight PET which uses the time-of-flight information of 511 keV gammas [14].

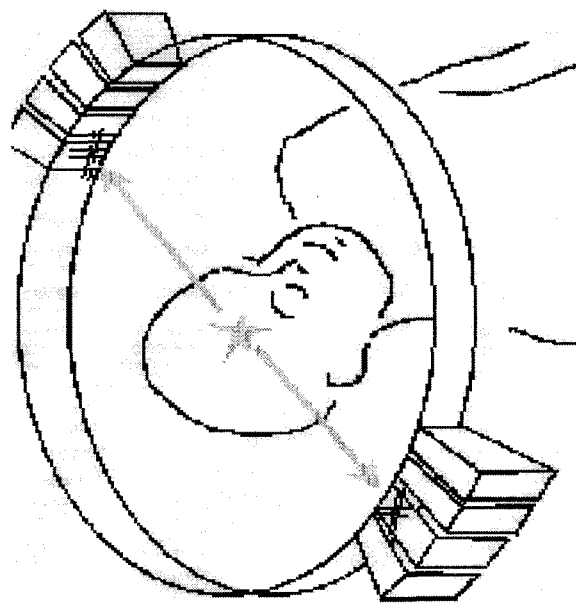


Figure 2.2: PET System

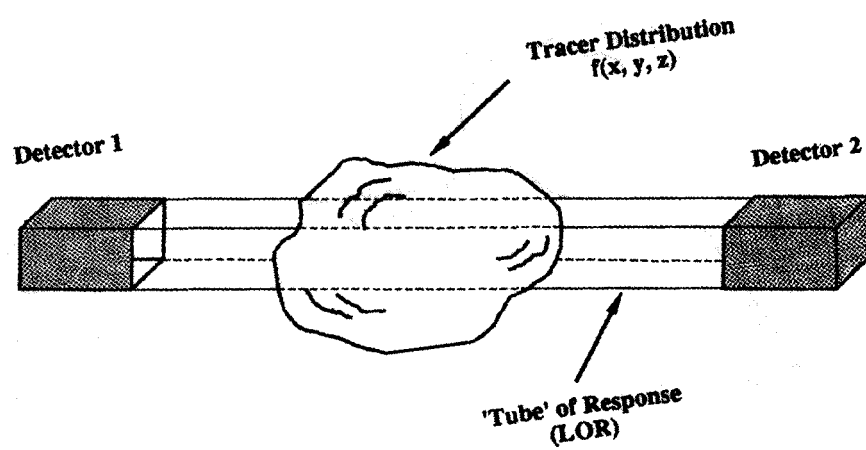


Figure 2.3: The Line of Response for two Detectors in Coincidence [12]

3. PET THEORY

3.1. Physics Behind PET - Particle Interactions

3.1.1. Particle Interactions with Matter

The detection of a particle is an ultimate result of an interaction process between the particle and the detector. Every radiation detector operates in a manner that depends on these specific interactions with its constituent sensitive material. Thus, for particle detection purposes, it is of great importance to know which basic processes occur when a particle encounters the detector and how the detector responds to these processes.

It is possible to classify particle types according to their interactions with matter together with their absorptions and detectability by a sensitive detector [15]. These are:

- Heavy charged particles (protons, mesons, heavy ions)
- Light charged particles (electrons and positrons)
- Electromagnetic radiation (gamma rays, X-rays, ...)
- Neutrons.

For now, we will only deal with light charged particles (electrons and positrons) and electromagnetic radiation (photons).

3.1.2. Electron-Positron Interactions with Matter

Electron and its antiparticle positron have the smallest mass among the charged particles and they have basically similar characteristics in terms of interacting with matter. When traversing a material, they lose energy by collision and ionization just as the other charged particles do. Furthermore, due to their small masses compared to other charged particles, they dissipate their energies by emitting electromagnetic radiation (bremsstrahlung). For heavier charged particles, probability for such a process is

negligibly small.

Ionization loss

When a charged particle enters a medium, it interacts electromagnetically with the atomic constituents of the material, i.e., nuclei and atomic electrons. It may either collide inelastically with an atomic electron which feels the electromagnetic field of the particle or scatter elastically from a nucleus. In these interactions (mainly collisions), the moving particle loses some of its energy and this energy is transferred to the absorber's electrons. This energy may be used up either to excite the atom by moving one of its inner electrons to a higher energy level (excitation) or to knock-out an electron from its atom (ionization). Therefore, the particle's kinetic energy will diminish in each of the collisions until it stops in the medium. The charged particle's direction of motion will be deflected by the collisions, but since the number of collisions are very high and their occurrence is a statistical process, the particle will keep its trajectory more or less the same. This case is true mainly for heavy charged particles. For electrons and positrons, the deflection is comparably large due to their small masses.

The stopping of charged particles in a material leads to the concept of range. *Range* may be thought as the distance in the specific material beyond which the particles with the same initial energy cannot penetrate. *Mean range* is then defined to be the thickness of the absorber material for which half of the incident particles are absorbed. From this, one can see that, the detection of a particle or the protection from radiation depends highly on the type and thickness of the medium used. It's interesting to know the average energy loss per unit length for each type of material by the particle. It's not wrong to talk about such a quantity if we assume that the fluctuations in the energy loss is small and the number of collisions is high. This quantity, mostly known as the *stopping power* or dE/dx , was first calculated by Bohr classically. The quantum mechanical version was done by Bethe and Bloch later on. The equation, known as the *Bethe-Bloch formula*, gives specific energy losses for heavy charged particles and it can be found in many standard textbooks [16, 17]. However, it needs to be modified for electrons and positrons due to their small masses.

For heavy charged particles, the specific energy losses will change as the kinetic energy of the particle changes. When the particle is at the end of its trajectory, dE/dx will attain its maximum value which forms the so-called *Bragg Peak*. This means that a particle will deposit the largest energy to the medium right before it stops [16].

Bremsstrahlung

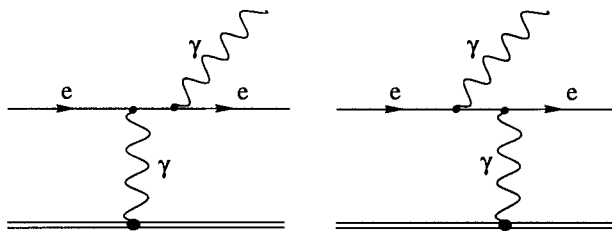


Figure 3.1: Lowest Order Feynman Diagrams for Bremsstrahlung

When an electron (or positron) passes through the electric field of the nucleus, it gains an acceleration (or deceleration) which results in an emission of radiation. The emission of photons is within a cone around the electron's direction of motion. This process is called bremsstrahlung (if within a magnetic field, called synchrotron radiation). Bremsstrahlung (radiation loss) is dominant over ionization loss at high energies of the electron. Below a critical initial electron energy, energy losses arise mostly from ionization. At the *critical energy*, $E_c \simeq 500/Z$ MeV, the energy loss due to ionization and due to radiation become equal [18]. Above that energy, radiation loss highly dominates. The above approximation states that the critical energy depends only on the Z of the absorber material and so is a characteristic parameter. In the high energy limit, the cross section for radiation loss can be given as

$$d\sigma \simeq Z^2 r_e^2 \frac{d\nu}{\nu} f(\epsilon, \eta, Z) \quad (3.1)$$

where Z is the atomic number of the material, r_e is the classical electron radius ($r_e = e^2/m_e c^2$) and ν is the emitted photon's frequency. In the function f , ϵ is the ratio of the initial electron energy to the final total electron energy, and η represents the effect due to the screening of the atomic electrons surrounding the nucleus. The

screening effect plays an important role in bremsstrahlung because it is the strength of the electric field between the electron and the nucleus that causes the emission and the more the nucleus is screened by the atomic electrons, the less the emission of photons will be. Thus, the energy spectrum of photons emitted due to bremsstrahlung depends on the screening effect of the atomic electrons on the moving particle. We should also note that, because of the r_e^2 factor, the emission probability goes like $1/m_e^2$. This explains why bremsstrahlung process is negligible for heavy particles. The probability reduces by a factor of 40000 even for muon, which is the next lightest charged particle.

The radiation energy loss is an integral of the cross section multiplied by the emitted photon energy over the allowable range and calculations in the high energy approximation lead to the result:

$$dE/dx = -E/x_0. \quad (3.2)$$

In this simple relation, E is the electron energy and x_0 is called the *radiation length* which is defined as the distance in which the electron energy is reduced to $1/e$ of itself due to radiation loss only. It is also a specific value for each material depending on their atomic properties [16].

Annihilation

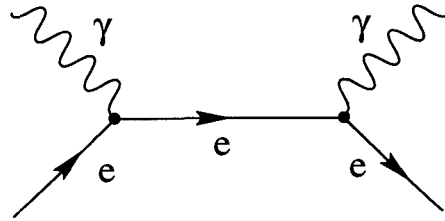


Figure 3.2: Feynman Diagram for e^+e^- Annihilation

For positrons, besides ionization and radiation loss, an additional process takes place which is called positron annihilation. Since a positron is an antiparticle, it ultimately annihilates into two photons with an electron in the medium. These photons

have a characteristic energy of 511 keV assuming that the positron annihilates with very little kinetic energy left and the electron is basically stationary. Thus, the energy involved in the process is just the rest masses of the e^+ and e^- couple and the two γ 's are produced with energies equal to 511 keV, the rest mass energy of electron. The reason for annihilation into two back-to-back γ 's is the conservation law for momentum. However, when the electron is bound, annihilation into a single photon is also possible but the cross section for this process is smaller than 20 per cent for that of 2- γ process [19]. The 2- γ annihilation cross section is given as:

$$\sigma = \pi r_e^2 \frac{1}{\lambda + 1} \left(\frac{\lambda^2 + 4\lambda + 1}{\lambda^2 - 1} \ln(\lambda + \sqrt{\lambda^2 - 1}) - \frac{\lambda + 3}{\sqrt{\lambda^2 - 1}} \right) \quad , \quad (3.3)$$

where $\lambda = E/m_e c^2$ with E as the total energy of the positron [20]. This cross section has its maximum value near $\lambda = 1$. This means that most of the time the annihilation takes place when the positron reaches small velocities via losing its energy by ionization and radiation along its path.

3.1.3. Photon Interactions with Matter

Among the particles interacting electromagnetically, photon is the most difficult one to detect. This is a consequence of the fact that they are non-ionizing particles, i.e., they don't lose energy by ionization: they are invisible to the detector as themselves. Instead, we can only detect their secondary products created during an interaction in the detector material. Therefore, it is crucial in gamma ray detection to know which interactions they undergo. The fact that photons are non-ionizing particles leads to the result that, due to the interactions, photons will be absorbed or be lost by scattering away which will cause an exponential decrease in the intensity of the photon beam along the absorber material. The number of particles, I , that have traversed a thickness of x in a material is related to the initial number of photons, I_0 , by the following exponential decrease:

$$I = I_0 e^{-\mu x} \quad (3.4)$$

where μ is called the *total or linear attenuation coefficient*. The inverse of this coefficient, μ , gives the *mean free path*, λ , which can be defined as the typical distance that a photon can travel without suffering a collision.

There are three processes that are the most dominant ones for typical energy ranges of radiation:

- *Photoelectric effect*: Predominant in the energy range 100 keV to 500 keV,
- *Compton scattering*: Important in the energy range 100 keV to 1 MeV,
- *Pair Production*: Possible (and dominant) when the photon energy is above 1.02 MeV.

Before a detailed study of the basic ones, a brief listing of the other processes by which gamma rays interact with matter is given below for the sake of completeness [21, 22]:

- *Rayleigh scattering*: Coherent scattering of gamma rays from bound atomic electrons, which is predominant at low photon energies, small scattering angles and high-Z absorbers.
- *Thomson scattering*: Coherent scattering of gamma rays by free electrons and by the whole nucleus.
- *Nuclear photodisintegration*: A type of process in which gamma rays are absorbed by nuclei and cause nucleons to be ejected. Such processes $((\gamma, n), (\gamma, p))$ occur only at very high gamma ray energies.
- *Nuclear resonance scattering*: This type of processes involve the energy levels of the nuclei which are excited by resonant absorption of gamma rays. This excitation results in the emission of gamma rays during de-excitation.
- *Delbruck scattering*: Scattering of photons by the Coulomb potential of the nucleus.

Photoelectric Effect

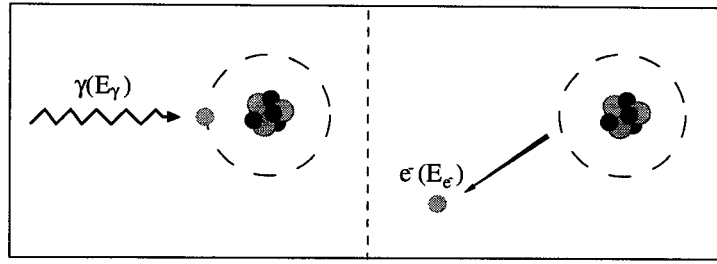


Figure 3.3: Photoelectric Effect: Photon in - Electron out!

It's possible for an incident photon to transfer all of its energy to the detector material by the interaction process called the photoelectric effect. In this process, a photon of energy, $E_\gamma = h\nu$, is absorbed by an atom which results in the ejection of a *photoelectron* most likely from the K-shell of the atom with a kinetic energy given by:

$$E_{e^-} = h\nu - W_{e^-} \quad (3.5)$$

where W_{e^-} is the binding energy of the electron. Although in the interaction the photon disappears and a photoelectron comes out, photoelectric effect involves the whole atom of the photoelectron. When the electron is ejected, the atom is left with a vacancy in one of its normally complete shells. The atom arranges itself so as to fill this vacancy by another electron from its outer shells or by capturing a free electron (if any) nearby. This replacement results in an emission of one (or more) characteristic X-ray photon(s). The energy of the X-ray is given by the difference between the binding energies of the photoelectron and of the filling electron. Characteristic X-rays may have an energy of the range of 1 keV to 100 keV; thus can travel a relatively small distance and can be photoelectrically absorbed by the detector again yielding a photoelectron.

In an alternative way, the binding energy may be liberated in the form of emission of one of the outer-shell electrons. This electron is called an Auger electron and has an energy equal to the difference between the atomic excitation energy, which is equal to the energy of the X-ray, and the binding energy of the Auger electron. Typical Auger

electrons have an energy of the order of a few keV.

Therefore, it's clearly seen that in photoelectric effect, all the incident gamma energy is used up in the creation of free electrons. In other words, the incident gamma radiation is totally converted into a secondary ionizing radiation in terms of electrons.

The photoelectric cross section depends on E_γ and the atomic number, Z , of the absorber material in a complex manner and cannot be easily expressed analytically. A rough approximation for photoelectric absorption per atom is

$$\sigma \simeq C \left(\frac{Z^n}{E_\gamma^{3.5}} \right) \quad (3.6)$$

where C is some constant and n is an exponent which varies between 4 and 5 [17]. It is interesting to note that the cross section goes as Z^4 or Z^5 , which makes the atomic number of the absorber material drastically important in building-up γ -ray detectors.

Compton Scattering:

Compton scattering is a process in which the incident gamma ray interacts with an electron in a material and scatters with the scattering angle, θ , as in the figure.

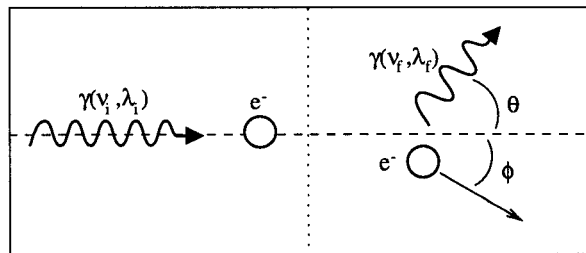


Figure 3.4: Compton Scattering

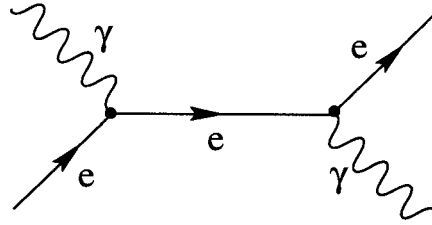


Figure 3.5: Feynman Diagram for Compton Scattering

The interaction, in principle, involves free electrons although the electrons in the material are in bound states. However, it's a very good approximation to consider them to be free when the energy of the photon is high with respect to the binding energy. Thus, one can treat the electron as free and apply the kinematic conservation laws to get some important relations. The energy of the scattered electron can be derived by solving the energy and momentum conservation equations simultaneously

$$h\nu' = \frac{h\nu}{1 + \epsilon(1 - \cos \theta)} \quad (3.7)$$

where $\epsilon \equiv h\nu/m_0c^2$ and m_0c^2 is the rest mass energy of the electron (0.511 MeV). The kinetic energy of the electron is also dependent on scattering angle θ as:

$$T = h\nu - h\nu' = m_0c^2 \frac{\epsilon^2(1 - \cos \theta)}{1 + \epsilon(1 - \cos \theta)}. \quad (3.8)$$

Examining the extreme case, $\theta = \pi$, one can figure out that the incident energy of the photon cannot be transferred to the electron totally. This case is the so-called backscattering of the photon and corresponds to the maximum kinetic energy that the electron can get with its recoil along the direction of incidence. This T_{max} of recoil electron is simply

$$T_{\max} = m_0c^2 \frac{2\epsilon^2}{1 + 2\epsilon}, \quad (3.9)$$

and leads to what is called a *Compton edge*. The cross section for Compton scattering was calculated quantum mechanically by Klein and Nishina (1929) [23]. The

Klein-Nishina Formula for the differential cross section gives the angular distribution of scattered gamma rays:

$$\frac{d\sigma}{d\Omega} = \frac{r_0^2}{2} \frac{1}{[1 + \epsilon(1 - \cos\theta)]^2} \left(1 + \cos^2\theta + \frac{\epsilon^2(1 - \cos\theta)^2}{1 + \epsilon(1 - \cos\theta)} \right) \quad (3.10)$$

where r_0 is the classical electron radius. The distribution yields the result that there is a strong tendency for forward scattering of gamma rays at very high incident energies.

Pair Production:

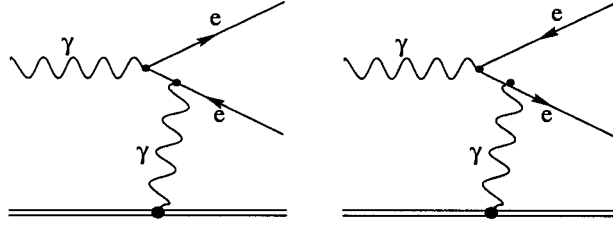


Figure 3.6: Lowest Order Feynman Diagrams for Pair Production.

A process which is possible to occur at photon energies higher than twice the rest mass energy of the electron and the positron ($2m_0c^2 = 1.022 \text{ MeV}$) is called *pair production*. Such an energetic gamma ray encountering a material may decay into an electron and a positron due to the coulomb field of the nucleus. Thus, a photon is absorbed and an electron-positron pair is created. The excess energy above the rest mass threshold is shared by the created pair as kinetic energies. Some small portion of the gamma ray energy is taken up by the nucleus for recoiling. In this way, the conservation laws for the system are satisfied. One can easily write the energy conservation as:

$$h\nu = 2m_0c^2 + T_{e^+} + T_{e^-} + E_{nucleus} \quad . \quad (3.11)$$

The positron produced in the process eventually annihilates and leads to two new photons as secondary products of the interaction. Together with bremsstrahlung process, pair production is mainly responsible for *electron-photon showers*, i.e., a bunch of particles increasing in number with each interaction and forming cascades. These secondary

productions and showers are important in radiation detection.

3.2. Scintillation and Scintillators

Scintillation is the conversion of the kinetic energy of the ionizing radiation to detectable light in a specific medium called *scintillator*. This mechanism is one of the basic tools for spectroscopic measurements and for detection of various radiation types. Scintillation occurs in two different ways: if the emission of visible light takes place right after the absorption of energy, it is called *fluorescence*; if it is delayed and is in a longer wavelength range, it is called *phosphorescence* or *afterglow*. Thus, most scintillators have two components in emission of the visible light. The prompt emission corresponds to a *fast* component which is of the order of 10^{-8} seconds and the delayed emission corresponds to a *slow* component of the order of 10^{-6} seconds in most scintillators. There are basically two major types of scintillator materials: organic (plastics, crystals and liquids) and inorganic (alkali halides and oxides) [15, 16].

3.2.1. Comparing Organic and Inorganic Scintillators

Structural Differences: Inorganic scintillators are crystals grown in high temperature furnaces and are made of alkali halides (i.e., NaI, CsI) or Oxides (i.e., BGO). They have scintillation properties by virtue of their crystalline structure. The transition of electrons in the energy states determined by the crystal lattice of the material (energy bands) is responsible for the scintillation mechanism in inorganic scintillators. Organic scintillators (plastics, liquids), on the contrary, are composed of aromatic hydrocarbons. Plastic scintillators are non-fluid solutions consisting of fluorescent organic compounds dissolved in a solidified polymer matrix. Organic scintillators scintillate on a molecular level unlike inorganic ones. In these materials, fluorescence process arises from transitions in the energy level structure of a single molecule. Therefore, basically each scintillator molecule can act as a scintillation center.

Interaction with Radiation: Besides their structural differences, inorganic and organic scintillators differ in their mode and level of interaction with ionizing radiation. For a typical X-ray/Gamma-ray energy range from 10 keV up to 1 MeV, the main interaction mechanisms involved are the Photoelectric effect and Compton scattering (figures 3.7,3.8). Inorganic scintillators are usually made of high Z-elements and have a fairly high density. High Z enhances the photoelectric interaction contribution, high density increases the interaction efficiency. The photoelectric contribution enables spectroscopic measurements. For example, NaI(Tl), due to its high Z component and high light output, can be used for detection of X-rays with energies as low as 5.9 keV.

In contrast, organic scintillators are made of low Z-elements and have a low density. Therefore, the main interaction mechanism is Compton scattering. The photoelectric effect is dominant only at low energies (typically below 20 keV). Because of the low density, more volume (thickness) is required to obtain a reasonable detection efficiency. However, the relatively low cost of Plastic Scintillators more than compensates for this when large area detectors are required.

The low intrinsic scintillation efficiency of organic scintillators results in rather weak pulses for photon energies below 100 keV. Standard plastic scintillators have a light output which is about a factor of 4 lower than that of NaI(Tl). The above energy limit can be lowered by using a low noise Photomultiplier Tube.

Applications: Inorganic scintillators are widely used in X-ray/Gamma-ray detection applications for which: 1. spectroscopy is needed, and/or 2. high detection efficiency is needed, and/or 3. low energy radiation has to be detected. Since they have high photoelectric contribution, i.e., good stopping power, they are mainly used where small-sized detectors are needed. However, most of inorganic scintillators need attentive handling and maintaining because their scintillation efficiencies are highly dependent on the environmental conditions. Inorganic scintillator based detectors are used in Nuclear Medicine (Gamma Cameras), Medical Imaging (CT scanners, PET scanners), Life Sciences (Thyroid Uptake), Radioprotection, (Space) Science, ...

As explained before, plastic scintillators are not very suitable for detection of lower energy X-rays and Gamma-rays and cannot be efficiently used for X-ray/Gamma-ray spectroscopy. However, they may be useful for Gamma-rays with energies above 100 keV. Their relatively low cost and availability as large size sheets make them ideal for such applications when a large detection area is needed. Plastic scintillators are also very useful for beta spectroscopy or fast neutron detection. Another interesting aspect of plastic scintillators is that they have very short scintillation decay times (a few ns), they are very good charged particle and neutron detectors, and they have good spectroscopic properties for these kinds of ionizing radiation. As a result, they are widely used in high energy and particle physics (calorimeters, time of flight (TOF) detectors) and in Radioprotection Equipment [29].

Some plastic scintillators are specially formulated to have a long decay time ($>200\text{ns}$). They are used in combination with normal, fast plastic scintillators for Phoswich detectors which can be used for Particle Identification through Pulse Shape Discriminating techniques [24]. Some Liquid Scintillators are very good for neutron-gamma separation; therefore, they are ideal for studying neutrons in a high gamma ray background.

3.2.2. A Type of Inorganic Scintillator: CsI(Tl)

In this section, we are going to list the properties of CsI crystal, especially CsI(Tl) that we will be using for our measurements. CsI is one of the few popular alkali halide crystal scintillators that have found application in many areas [25]. One of the reasons for that is the rugged and plastic-like nature of these crystals which makes them resistant to mechanical shock. A drawback of pure CsI is its steep dependence of the light yield on temperature [26]. CsI is used as pure crystal or is activated with Sodium or Thallium which is a heavy metal. Basic physical characteristics of these three types of crystals are mostly the same. However, for scintillation properties, they differ depending on the type and the concentration of the activators. In terms of usage, pure CsI and CsI(Tl) are only slightly hygroscopic, i.e., the surface of the crystal may degrade when kept in humidity.

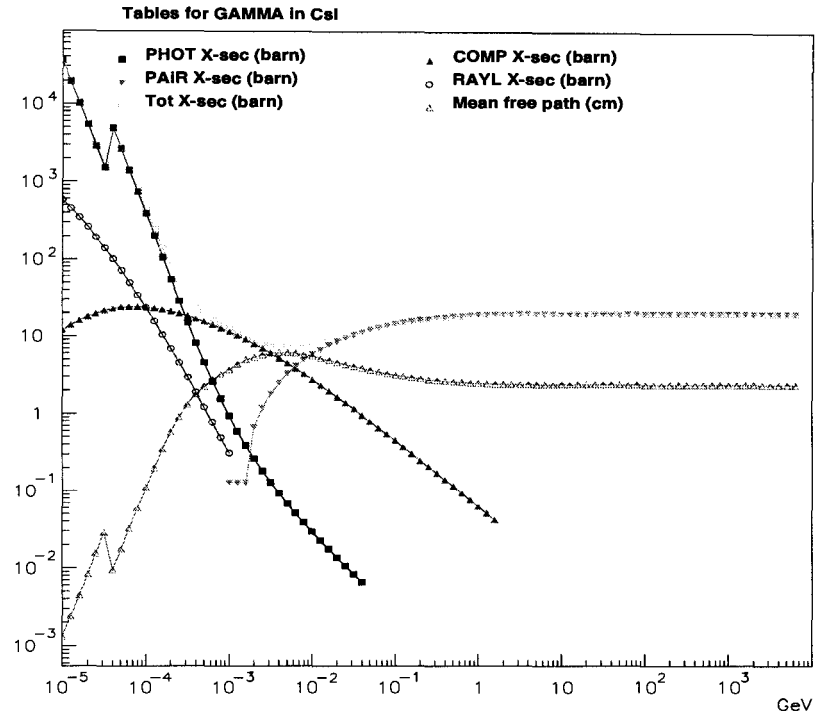


Figure 3.7: Cross Section Plots for CsI

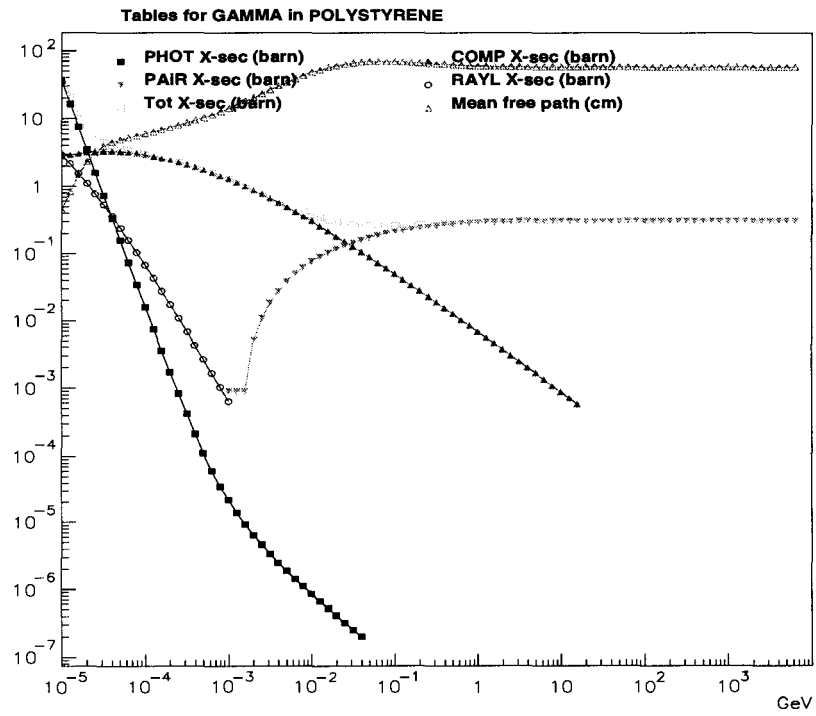


Figure 3.8: Cross Section Plots for Polystyrene

CsI is a high density material with a high Z value which enhances the photoelectric absorption. When activated with Thallium impurities, it gains a high light output capacity. CsI(Tl) is known to have the highest light output among other crystals and has the shortest radiation length when compared to common scintillators such as BGO [27]. However, its maximum emission wavelength is at 550 nm which makes it not so suitable for alkali photocathode photomultiplier tubes. Anyhow, the photoelectric yield of CsI(Tl) is about 10 times that of undoped CsI. The relative light output vs temperature curve shows that CsI(Tl) has its optimum values between 20-50 degrees Celsius which makes it well-suited for room temperature applications. The decay time of CsI(Tl) has, as many of the other crystal scintillators, more than one components. Its fastest component has a value of about 600 ns and the slowest is 3.5 μ s. For gamma rays, its average decay time is about 1 μ s [28]. In this manner, CsI(Tl) may not be very suitable for fast timing requirements. However, the light output of CsI(Tl) is quite high when compared to NaI(Tl) (table 3.1).

3.3. PET requirements

3.3.1. PET Detector Requirements

Like in every modality in nuclear medicine, it's also necessary in PET to meet some requirements to increase the efficiency of detection. This is needed to enhance the imaging quality which will increase the reliability in clinical diagnosis. An ideal PET system would have [5, 30]:

- high spatial resolution (≤ 1 mm),
- good timing resolution (≤ 5 ns fwhm),
- high intrinsic detection efficiency (> 50 %),
- high energy resolution (≤ 10 %),
- high detection speed, i.e., low dead time (< 4 μ s inch²) in terms of detector time and front surface area

- larger detection area to cover human body,
- high sensitivity,
- efficient quantitation of uptaken radioactivity,
- low cost,
- good and reliable 2-D/3-D images.

The factors that contribute to a PET detector's spatial resolution are given as FWHM values below [5, 31]:

- Positron range: 0.5-2 mm depending on the endpoint energy (T_{max}) of the source.
- Photon acolinearity: ± 0.25 degrees of angular deviation from 180 degrees gives 1-2 mm error for a detector ring diameter of 50-80 cm.
- Detector geometry: a detector with front surface area (cross section) of 3 mm contributes an error of 1.5 mm in resolution.

3.3.2. PET Scintillator Requirements

Being the most important part of the PET detector system, an optimization in the utilization of scintillator material is needed while constructing the system. Listed in approximate order of decreasing importance, below items are favoured to meet the requirements to get the best results in PET [32].

- Good stopping power:
 - Short attenuation length (< 1.5 cm). It is claimed that the image quality is enhanced when the crystal length is about three times the attenuation length. This is mainly needed for the prevention of the radial elongation effect which can also be cured by depth of interaction measurement [9],
 - High photoelectric fraction over Compton scattering (> 30 per cent), i.e., high effective atomic number which improves photoelectric interaction probability,

- Short decay lifetime (< 500 ns). This affects both timing resolution and the dead time,
- High light output (> 8000 photons per MeV),
- Durability,
- Low cost (< 20 dollars per cm^3).

Table 3.1: Comparison Table for Scintillators

	CsI(pure)	CsI(Tl)	NaI	BGO	Plastic
Density (g/cm^3)	4.53	4.53	3.67	7.13	1.032
Primary decay time (ns)	16	1000	230	300	2.4
Afterglow (after $6\mu\text{s}$) (%)	–	0.5-5.0	0.3-5.0	0.005^4	–
Light output (phot/MeV)	2×10^3	54×10^3	38×10^3	10×10^3	1×10^4
Attenuation Len. (511 keV)(cm)	2.27	2.27	2.94	1.08	N/A
Radiation Length (cm)	1.85	1.85	2.59	1.12	42.4
Photoelect. Yield (% of NaI(Tl))	4-6	45	100	15-20	28
Emission Wavelength (max) (nm)	315	550	415	480	423
Refraction Index (emission max)	1.95	1.79	1.775	2.15	1.581
dE/dX (min) ($\text{MeV}/(\text{g}/\text{cm}^2)$)	1.24	1.24	1.30	1.25	1.94
Hygroscopic	Slightly	Slightly	Yes	No	No

⁴after $3\mu\text{s}$

4. OVERVIEW OF GEANT, A MONTE CARLO SIMULATION PACKAGE

GEANT (version 3.21) [33] is a Fortran-based program package which simulates the passage of elementary particles through matter by using standard Monte Carlo approach. Originally designed for High Energy Physics experiments, it is used to simulate the machine parts of the experiment, namely the detector and its components. It is also possible to apply GEANT to many other areas such as medical and biological sciences. GEANT can be used to track any of the (GEANT-tabulated) particles step by step within a specific medium and to view its trajectory inside the detector. It's important to note that GEANT can be used only if the CERNLIB [34] package is installed on the computing system. There is also a Motif-based graphical user interface (GUI) available in the interactive version of GEANT: GEANT++. This feature makes it easier for the user to directly observe what's happening inside the detector, to take immediate action and to debug the setup or the program codes if necessary.

GEANT allows the user to implement codes depending on his applications. This is made possible through the subroutines reserved for the user. These files are differentiated by their first two letters which are either GU or UG. The user is expected to write the code pieces describing the experimental environment, i.e., the detector and surroundings, to assemble the program segments to make it an executable program so as to get the desired output from the simulation. One can control the simulation externally by using data cards for the program to read during the initialization process.

Usually, the user will want to store and gather information from data structures (banks) or to read and write to data files. GEANT data structures are stored physically in the /GCBANK/ common block. These data structures also control the communication between program segments of the whole system. To handle data and banks a CERNLIB package, ZEBRA [35], is used. ZEBRA system allows dynamic data structuring at execution time and manipulation of various kinds of data by means of common

blocks and pointers to the data structures. The user may also want to book and fill histograms. For histogramming and analysis purposes, another CERNLIB package, HBOOK [36], can be utilized. It is possible to call HBOOK during the simulation just as any other CERNLIB packages. It is the main package to book and fill histograms, to do statistical analysis and function fitting to any data. Graphical outputs and plots are done with PAW (or PAW++). In fact, data analysis can be done just by using PAW [37] which is a tool that integrates all the functionalities of the HBOOK and ZEBRA with other CERNLIB packages to provide a complete interactive working environment to the user.

4.1. Geometry and Physical Parameters

GEANT has a master reference system in 3 dimensional cartesian coordinates (MARS). Each time a volume is specified in GEANT, it automatically has its own reference system. If a volume is to be contained within another volume, the latter is called a “mother” reference system (MRS). The former is positioned with respect to MRS and is called a “daughter” and it is a daughter reference system (DRS) with respect to MRS. For the orientation of the daughter in the mother, transformation vectors and rotation matrices are used. The rotation matrices can be developed by defining the polar and azimuthal angles of the axes of the DRS in the MRS via a call to the GSROTM subroutine and the volume is positioned accordingly. If a number of copies of the same volume is to be placed in the same mother, the copies are differentiated by a unique number assigned to each one of them. Overlapping of volumes may also be made possible by using the necessary flags. One can also define new volumes implicitly, by dividing the mother into a number of cells. The data structure for volume parameters are kept in JVOLUM structure.

The physical properties of volumes are implemented by parameterizing the material that fills the volume. The standard material constants are contained in the JMATE data structure including the atomic parameters, the density of the material (in gr/cm^3) and the radiation length (in cm). GEANT has 16 materials already implemented in this data structure. Sometimes the user may want to define his own mixture or com-

pound. In this case, a call to routine GSMIXT is needed.

There are some parameters related to the tracking of the particles in a chosen material. They are called the *tracking parameters* and are defined in GSTMED. In this routine, one can set the *sensitivity* parameter of a volume to define it as a detector, the maximum fractional energy loss in one step, minimum and maximum size permitted for one step (in cm), turn on/off the magnetic field (in kGauss) within the volume, and the accuracy of passing through the interface of two neighboring mediums. By setting such parameters, the material becomes a *tracking medium*. It is basically these parameters that give the material the properties on which the results of the simulation depend heavily. Every GEANT volume must be associated to an existing tracking medium stored in the bank pointed by JTMED structure.

4.2. GEANT Particles and Processes

GEANT contains most of the known particles and ions that can be tracked throughout the simulation. The parameters belonging to the particles, such as their masses (in GeV), lifetimes (in seconds) and charges (in units of electron charge), are stored in JPART data structure via GSPART routine. By using the same routine, the user is allowed to define his own particles or redefine the already existing ones. However, this should be done with extreme care to avoid complications in simulation. For the unstable particles, GEANT stores the decay modes and branching ratios for two and three body decays through the routine GSDK in the data structure JPART. Prior to a call to GSDK, the definitions of the decaying particle and the secondaries should be done.

Most of the physical processes are included in GEANT according to particle types. These can be classified as: electromagnetic processes, multiple scattering, hadronic interactions, muon interactions, and decays in flight. However, scintillation mechanism is not yet implemented in GEANT 3.21. GEANT can simulate electromagnetic processes within the 10 keV to 10 TeV energy range. For hadronic interactions the lower limit is about a few tens of MeV. A complete listing of processes implemented in GEANT

is given in Appendix C.

4.3. Flowchart and Tracking Process

GEANT package has three phases during the run: initialization, event processing, termination.

The initialization stage is controlled by the user code, UGINIT (fig. 4.1). The GEANT common blocks are initialized, the data files are opened, the data records are read and histograms are booked all at this stage. The definition of the volumes and media are done via UGEOM and the filling of energy loss tables and cross sections (GPHYSI) take place also at this point to start the event processing stage.

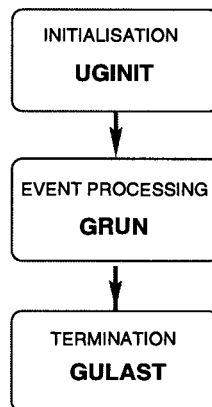


Figure 4.1: Over-simplified GEANT Flowchart

The event processing is triggered by a call to GRUN which is responsible for the tracking of particles in the media. The event initialization is done by GTRIGI and each event is processed by GTRIG. To generate and/or read the kinematics for the primary track, GUKINE is called.

The last phase of the run is the termination stage which is again controlled by the user via the routine GULAST. In GULAST, a call to GLAST makes it possible to print

some statistical information about the run.

The basic part of GEANT after the definitions of the geometry is the tracking of the particles through this defined geometry. In general, simulation of the tracking of a particle is predicting the spatial coordinates of its trajectory and computing the momentum coordinates at each point by integrating the equations of motion on successive steps from one trajectory to the next. Thus, a critical parameter is the step size of a particle which should be *a priori* estimated. Tracking is done at the event processing stage, under GRUN, by the appropriate calls to GEANT routines. At event level, tracking is controlled by GTREVE which loops over all vertices and stores all tracks from the current vertex in the temporary stack JSTACK. It controls propagation of each particle through the media via calls to GTRAK which can be called by GUTRAK. Tracking of each particle is type-dependent which necessitates different routines to be called for different particles. As an example, for electrons the routine GTELEC is called, whereas for photons, the name of the special routine used is GTGAMA. The subroutine GTRACK tracks a particle until one of its possible ends: decaying, interacting, falling below the energy threshold (kinematic cuts set by the user or the default values) or escaping from the MARS.

Within the tracking loop, there is a subroutine, GUSTEP, called at the end of every step of the particle. This routine is very important in taking actions for the run. The user may require the current track parameters that are stored in the common block /GCTRAK/. These include, for example, the energy loss for the current step and the history of the step. GUSTEP is also mainly used for recording the hits in the data structure JHITS and space points in the data structure JXYZ. If any secondaries are generated during the event, their informations are stored in the common block /GCKING/. The user may choose to discard these secondaries fully or store them in the data structures to be tracked by calling GSKING in GUSTEP. One thing to keep in mind is that, in fetching a new particle in a given event, GEANT chooses the last generated particle before the first one (Last In - First Out).

A typical algorithm for simulating the behavior of particles in an experimental

setup with GEANT would be like this: The user defines a geometry, first creating each element of the setup by defining volumes in the user-reserved subroutine UGEOM. The volumes can be constructed by using the standard GEANT geometric shapes, such as box, tube, sphere and some others. In the same subroutine, the material and tracking parameter definitions for each volume are also to be completed. The material selection can be done through the data cards at initialization time. Once the definition of volumes and of their physical properties are finished, the positioning of the daughter volumes into their mothers can be done via GSPOS routine can be done. After the geometry definition, to investigate the physics in this geometry by tracking generated particles, the user implements necessary algorithms in user-reserved subroutines such as GUSTEP, GUTRAK and GUKINE. The generation of the primary track for this purpose is also done in GUKINE. For this, the phase space components of the primary beam particle is to be given in data records. Also to be set in data cards are the switches for interaction types and kinematic cuts for particle types.

5. SIMULATION OF THE PET UNIT

It's generally favorable first to simulate an experiment if possible and then to perform it according to the results of the simulation. In this section, we will try to describe a Monte Carlo simulation done by using the GEANT detector simulation package for our sample PET coincidence detector unit. Although we did not implement all the features of our setup in this simulation and use all facilities of GEANT such as digitization, it provides enough information about the behaviour of the CsI scintillator crystals and about coincidence conditions. One more thing to keep in mind is that the simulations may yield only very idealistic results since the effects of systematical and statistical errors in data-taking are not included in our simulation program.

5.1. Setup Description

The system that we simulated with GEANT mainly consists of three parts: two scintillator block matrices made of individual scintillator sticks covered with Teflon and an encapsulation in which the pointlike positron source was placed. The geometric tree structure of the system can be seen in figure 5.1. First of all, we defined the mother volume to be a “universe” box with dimensions $50 \times 50 \times 50 \text{ cm}^3$ and with its medium as air. Air is already implemented in GEANT as a material. Taking this mother volume as the master reference system for positioning, we could orient our daughter volumes which are obviously the block matrices and the source encapsulation. We placed the encapsulation right at the origin of the universe and the scintillator blocks 15 cm apart from each other and face-to-face at 180 degrees to make them potentially coincident for back-to-back scattering of photons that emerge from the encapsulation.

To make a 2×8 matrix of scintillators, we created, in subroutine UGEOM, the volume “TEFL” which is the scintillator sticks covered with $150 \text{ }\mu\text{m}$ teflon and we produced 16 identical copies of it. “TEFL” is the mother of the volume “SCIN” which describes the scintillator stick. Each stick is $3 \times 3 \times 30 \text{ mm}^3$ in size. The size is specified so as to make them identical to the scintillators used in data-taking. Around the 2×8

matrix of TEFL, there is also another layer of teflon 150 μm thick. Altogether they make up the scintillator matrix, which is referred to as “UNIT” within the code (fig. 5.2). Although the PSPMT was not implemented in the simulation, the back sides of the matrices were kept free from teflon since it would be the face that is to couple to the PSPMT.

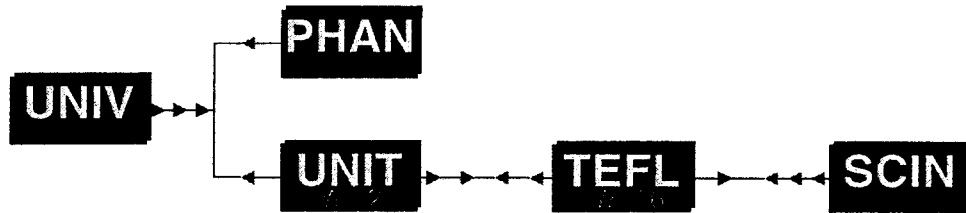


Figure 5.1: Geometric Tree Structure of the System Simulated with GEANT

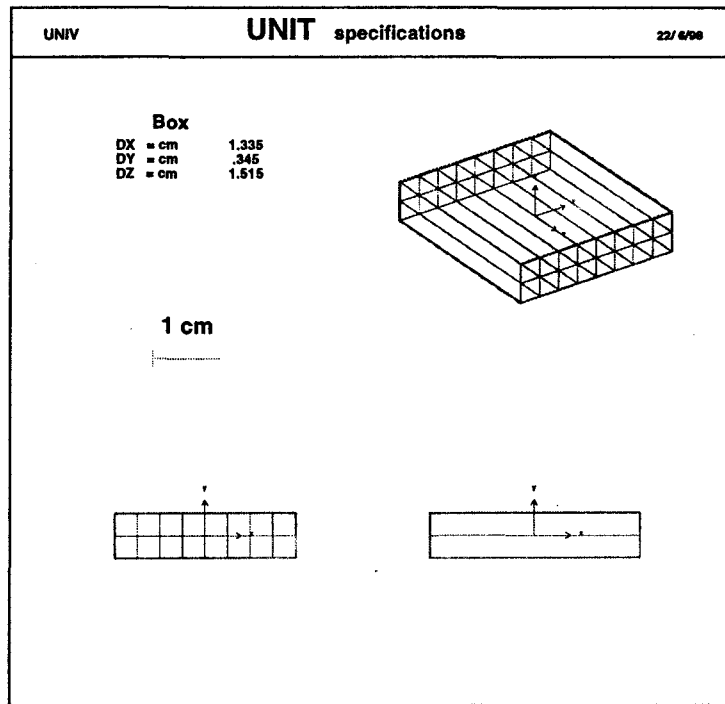


Figure 5.2: Scintillator Block as Specified in GEANT

In between these units, we located the source encapsulated with polystyrene with dimensions 25x6x4 mm³. The size is comparable to the encapsulation of the ²²Na

source that we used for data-taking and polystyrene is chosen to imitate the material of the encapsulation.

5.2. Simulations and Analysis

There were mainly two interesting aspects for us to analyze in this geometry: the interactions of 511 keV gamma rays with CsI crystals and the occurrence of coincidence. So, we implemented the simulation algorithms accordingly.

A perspective view of the system simulated by GEANT is seen in figure 5.3. In this picture, the positrons with energies of 350 keV are created at (0.9, 0, 0) point and their momentum directions are distributed uniformly in full solid angle. The tracks for back-to-back gammas coming from annihilation are drawn for five events. One of the photons is observed to have undergone photoelectric absorption in UNIT1. This volume, UNIT1, was located at (0, 0, -9) cm and was chosen to represent the matrix yielding the position information.

For the analysis of 511 keV gamma ray interactions in CsI crystals, the positrons were created at the center of the system. The positrons can not, but the gammas usually can, escape from the polystyrene so we basically illuminated the front surface of the UNIT1 with these gammas. From then on, whenever a gamma interacted within the scintillator medium and generated an electron, we histogrammed the deposited energy. In addition, we differentiated photoelectric effect from Compton effect to see the contribution coming from photoelectric effect since it's known that CsI (and other dense inorganic crystal scintillators) are preferred for their high photoelectric interaction probability. Figure 5.4 shows the total energy distribution of generated electrons (excluding Auger electrons) and photoelectric contribution to this distribution (blue foreground in fig. 5.4). There is a clear distinction of photoelectric peak at about 470 keV from Compton continuum and other photoelectric peaks occur at about 150 and 25 keV. The Compton edge is also seen to occur at 350 keV and the effects of multiple scattering is observed inbetween the photoelectric peak and the Compton edge. However, in real data-taking this ideal picture will be smeared out.

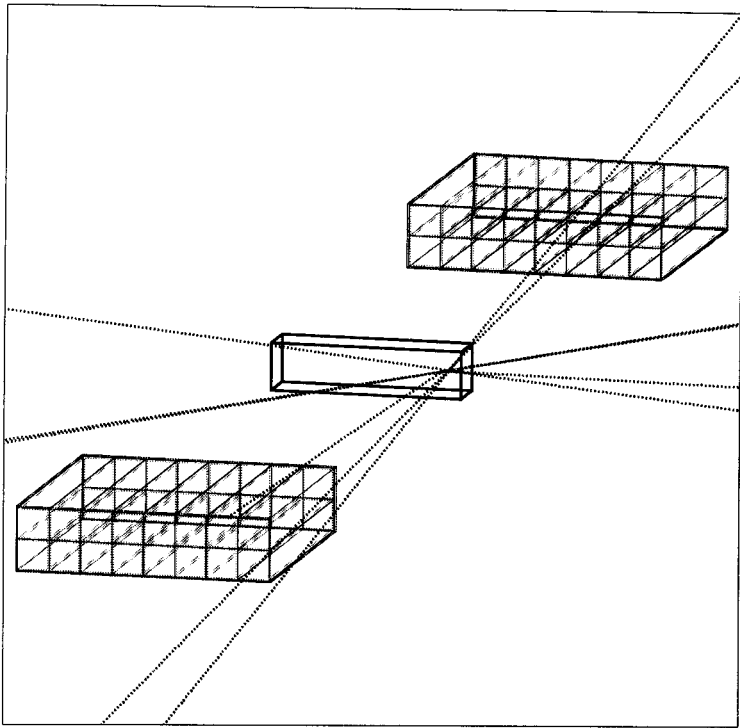


Figure 5.3: A Perspective View of the System Simulated with GEANT

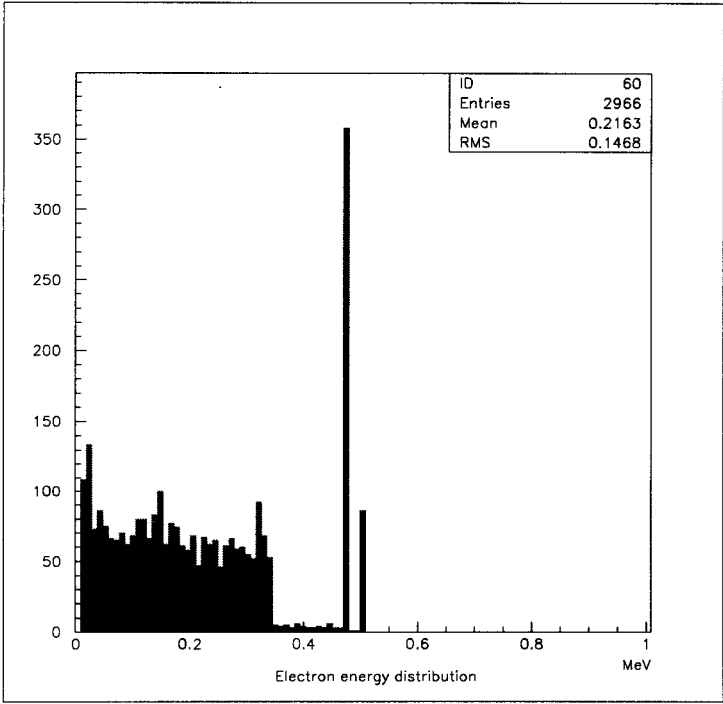


Figure 5.4: Electron Energy Distribution

Another important factor in gamma ray detection is the consequences that arises from the Compton scattering of the initial photon which undergoes a second interaction within the same detector. This may lead to false triggering and/or false pulse height determination. To examine this kind of crosstalk for our CsI crystals, we have chosen a crystal to target 511 keV gammas. We have not generated positrons for this case but just 511 keV gammas with their momentum directions fixed to the center of the crystal number 13 which can be seen in figure 5.5. Each crystal is represented by the channel numbers, as specified and all other parts of the setup were kept as before. Figure 5.5 shows the crystals in which a gamma interaction has occurred during the simulation. For this specific case, we calculated the ratio of the scattered hits to the initial hits in crystal number 13. That ratio turned out to be about 16 per cent with most of the contribution coming from the nearest neighbors of that channel.

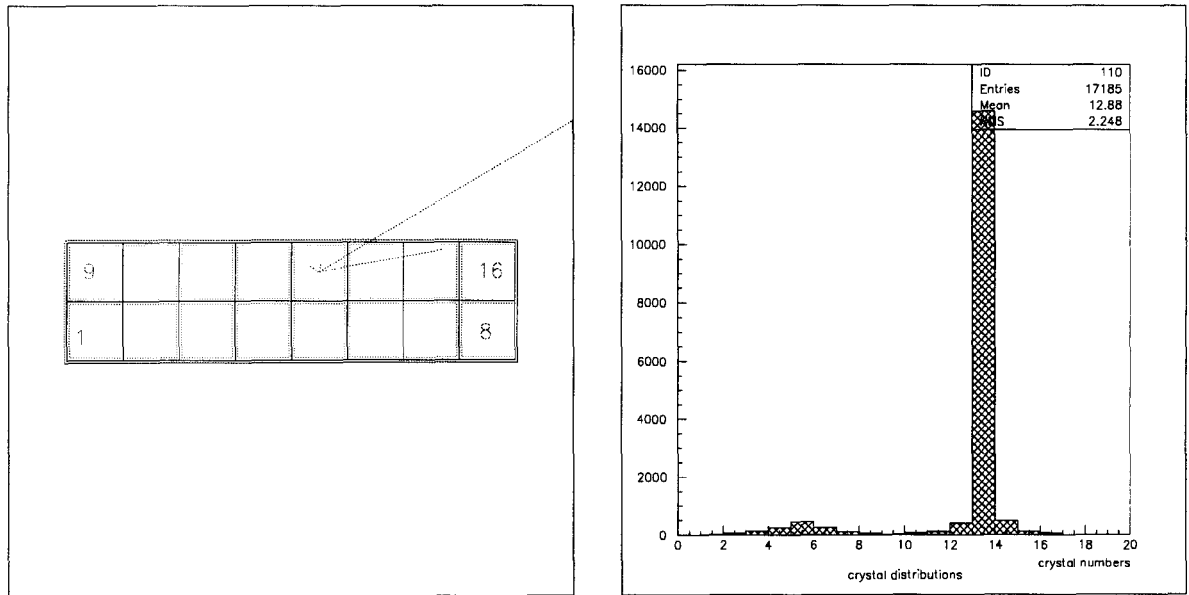


Figure 5.5: Cross Sectional View of UNIT and Crosstalk at Gamma Interaction Level

For the analysis of coincidence, we have chosen to analyze two different initial vertex points along the x-transverse direction: at the very center and with a shift of 0.9 cm in positive x direction, which is in front of the 14th crystal. We constructed the coincidence algorithm in routine GUSTEP such that whenever we get a signal from both of the matrices at one single event, we considered it as a coincident hit, provided that the gammas are the products of the annihilation process. The distribution of these

hits is seen in figure 5.6.

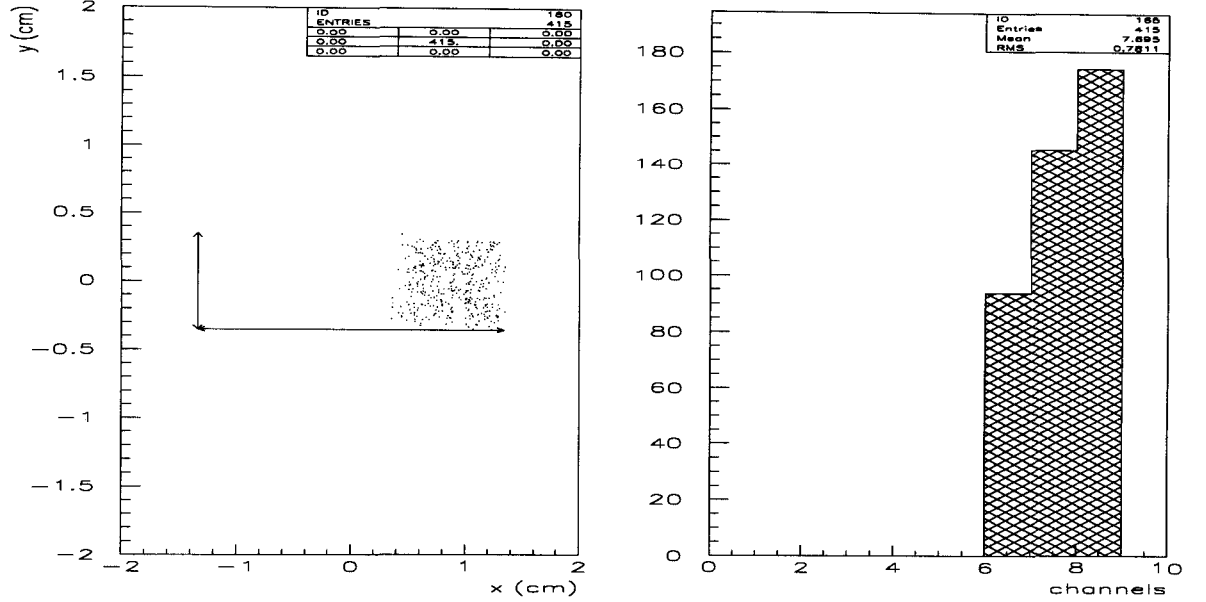


Figure 5.6: Results for $x=0.9$ cm

Figure 5.6 also illustrates the distribution of coincidence hits on the plane parallel to the matrix faces (x-y plane). Arrows approximately outline the UNIT matrix. For this exemplary simulation, total number of gamma ray interactions within any crystal is 2139 even for out of a million positrons generated. Out of this number, only 415 of them were coincident, i.e., a 20 per cent. However, it is useful to keep in mind that the solid angle seen by the matrices is very small which effects the number of occurrences and that the spatial window defined by the source location is very effective in recording coincidences.

The simulation was also performed with the scintillator material being polystyrene. For the same number of primary positrons generated at the center point and for totally the same conditions, we saw that no coincidence was observed. More than that, not a single interaction took place in any one of the UNITs. This means that it should take a longer time if coincidence is expected with polystyrene. This gives a clue on

why inorganic scintillators are more advantageous to use than organic scintillators in PET. Furthermore, in such materials one would expect to see more contribution from Compton scattering and less contribution from photoelectric effect, which is again undesirable since nearly full energy deposition comes from the contribution of the latter.

6. DATA TAKING AND ANALYSIS

6.1. General Description

In this section, we are going to describe the three basic measurements that were performed. The first one is a general system response and stability measurement. In this measurement, we expected to have an idea on the level of the crosstalk within the system we were using. The second one is a spectroscopy experiment performed with crystal scintillator pieces (CsI(Tl)) and plastic scintillators (NE102) using different radioactive sources. Thus, we had the opportunity to compare these two different detector materials. The main measurements were, of course, the examination of our single PET detector coincidence unit by taking data with a 2x8 matrix of CsI crystals.

Before going into the details of the different measurements performed, we will give a description of the general hardware setup, the DAQ system, and the specifications of read-out components used. We had three photomultiplier tubes (PMT) to be used in data-taking. The first two were single anode PMTs: Hamamatsu R1166, 1.9 cm in diameter and EMI 9839A, 5.0 cm in diameter. They were used as test and trigger counters. The third one was a position sensitive PMT (PSPMT) (Hamamatsu R2486). It was a cross-wired multianode PSPMT [38] of 16 X+16 Y channels with the pitch size between the wires 3.86 mm [39]. The negative signals from the PSPMT anode wires were preamplified before reaching the readout modules. The preamplifier used for this purpose produced positive signals. So a low-noise inverter board was used to invert the polarity of these signals. The high voltage for the PSPMT was supplied by a Fluke-413D, whereas the other PMTs were powered by an ORTEC 556.

In order to read-out from the PMT's and to drive the logic of the DAQ, we had both CAMAC and NIM crates in operation. On the CAMAC crate, we had three ADCs two of which were LeCROY 2249 A, 10 bits. The last one was a LeCROY 2249W, 11 bits, and all had 12 independent readout channels. The conversion rate for these ADC's were 0.25 pC/count.

The CAMAC system communicated with a Linux-operated [40] PC (i586) through the GPIB interface. For this purpose, LeCroy 8901A CAMAC controller with GPIB interface and a 16 bit National Instruments (NI 488.2) GPIB card mounted on the PC were used. GPIB libraries and device drivers for I/O hardware interface under LINUX were developed by C. Schröter [41].

The code utilized for DAQ was locally written in C language and was supported by a Tcl/Tk graphical user interface (GUI). The program, with the GUI, is a “multi-purpose” program which eased the operation and adaptation to various kind of experiments. It can be used to register data from different CAMAC modules such as ADC and TDC with the possibility of specifying channel readout order, to do on-line histogramming, ... The code for this program is given in Appendix E.

Two step motors were used in scanning measurement to allow precise motion on a horizontal (X-Y) plane. Both of these motors were 2.4 A bipolar stepping motors (EVER Elettronica, Power Max II model 23PM 220118M8) with 200 steps/revolution. We used a microcontroller (EVER Elettronica, model MPP10) to adjust and control the step sizes in X and Y directions. These step motors were also controlled by the same i586 via the standard parallel port using a locally produced program (in C language) and the appropriate device driver [42].

6.2. Test of the PSPMT and Crosstalk Measurement

In this measurement, our aim was to estimate the amount of the signal detected by the adjacent wires when a single wire in PSPMT was hit. For this purpose, we performed a 2-D scanning measurement for which we used a stable signal of known amplitude and shape. The signal was created by a pulse generator (HP 8007B) and was a negative square pulse with an amplitude of 2.10 Volts and 44 ns width as seen in figure 6.1.

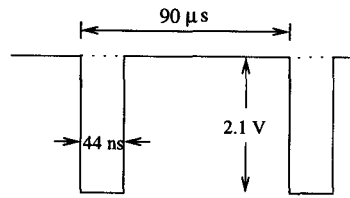


Figure 6.1: Signal Shape

The signal was then sent to an LED pulser to illuminate the PSPMT surface through a pointlike window. Triggering was also taken care of by the trigger output (+1.8V) of the same generator. Some delay had to be applied to meet the “sit-in-the-gate” criterium of the ADCs for the PSPMT response signal. The gate signal (NIM standard, -800 mV) was obtained by a discriminator with threshold set at -70 mV and width at about 100 ns. Since we were using a PSPMT with 32 channels, three ADC modules (all 10 bits) in the CAMAC crate were needed to read-out from all these channels simultaneously (fig. 6.2). The operating voltage for the PSPMT (R2486) was -1250V DC which is the optimal value. The PSPMT preamplifier voltage was at the point where it had the maximum allowed value (6.50 V) without operating in avalanche generation mode [43].

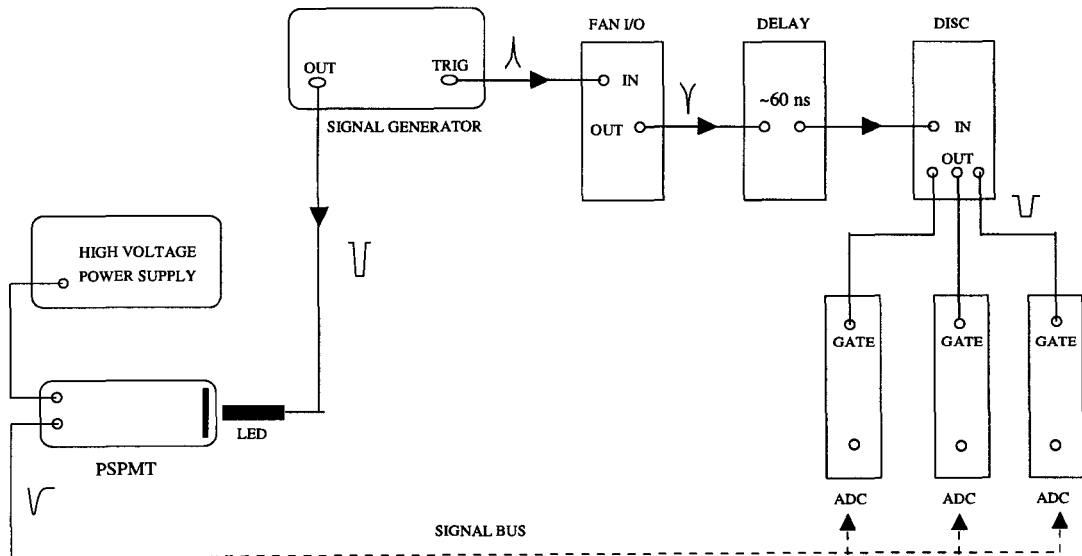


Figure 6.2: Setup for the Crosstalk Measurement

The scanning process was made possible by the step motors described in the previous section. They were mounted in the light-tight box in which the light-sensitive detection units were kept during the experiments. The PSPMT was held vertically up so that the step motors that were responsible for the motion of the LED could perform a proper 2-D surface scan. The scanning was confined to a rectangular region ($20 \times 26 \text{ mm}^2$ in area) on the PMT shielding window over its surface. This confinement was favoured for reducing time consumption, since only the middle region of the PSPMT surface would be needed for later measurements with the sample PET detector unit.

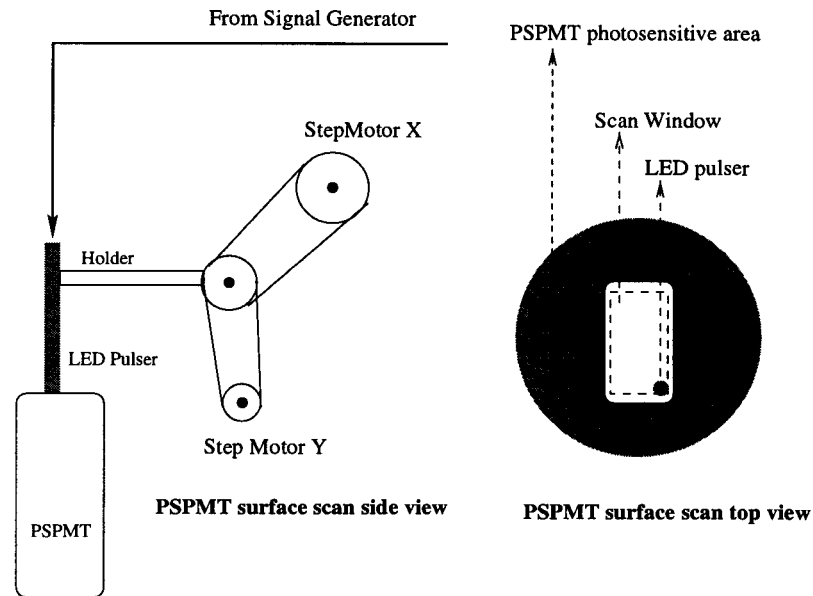


Figure 6.3: General View of the Surface Scan Setup

The initialization point for the scan was the bottom-right corner of the PMT window which we called the 0-0 point (fig. 6.3). At that position, we started our program that automated the data-taking. The program consists basically of a loop that calls motor-controlling program and the DAQ program in sequence. We took data of 4000 events at each x-y point and moved to the next point which is approximately 1 mm (for motor Y, $988 \mu\text{m}$ and for motor X, $998 \mu\text{m}$) apart on the surface of the PSPMT. This distance corresponded to 38 steps in Y direction and 640 steps in X direction. In this way, we collected data for 209 distinct points. These points were named with the

corresponding steps, for example, the first scan point was 0-0, whereas the last one was 684-6400.

We then off-line analyzed the raw data taken at each scan point. We wanted to apply cluster analysis and center of gravity algorithms to be able to determine the wire positions, so we wrote a C code for this purpose (presented in Appendix E). This code allowed us to see the raw data and analyze it at the same time depending on the desired usage. In the analysis, our aim was to get as much statistics as we could while satisfying the center of gravity algorithm requirements.

6.2.1. Analysis

The PSPMT system responds to the source in such a way that it may give signal from more than one if its 16 X and 16 Y channels. This is due to three main reasons:

1. There may be internal crosstalk factors, such as the spreading of the photo-electrons causing a shower (cloud) in dynodes until they reach the anode wires, thus generating signals covering multiple channels. In fact, this factor is mostly inevitable in such PSPMTs.
2. The source itself or the source light may be covering a larger area than the spacing between the wires. This gives rise to an external crosstalk.
3. Another crosstalk reason can be due to the preamplifier circuitry that is used to amplify the signal from the PSPMT channels.

Therefore, what one usually expects to observe in read-out is a group of adjacent channels in both X and Y directions with non-negligible pulse heights (PH). Such a group is called a *cluster*. A typical cluster is made up of a central channel with maximum pulse height plus two (or more) adjacent channels with pulse heights high enough to differentiate from the noise pulse heights. A cluster is characterized by its length. The cluster length is the number of channels that fall within a cluster. After determining the cluster, one can start *center of gravity* calculation for each event. This is

done by weighting each channel in the cluster by its pulse height.

In our analysis, we constrained ourselves to those events in which only one validated cluster existed both in X and Y, which is equal to say that the *cluster multiplicity* for all accepted events was one. The cluster was a valid one when it had a length between two and six channels, inclusive, and contained the channel with the maximum pulse height. A channel is accepted to be in a cluster if its pulse height is bigger than 2 per cent (~ 20 ADC counts) of the maximum possible PH which is 1024 for our ADC's. It's useful to note that the subtraction of ADC pedestal and normalization of each channel's data by a coefficient predetermined by a calibration measurement was also handled in the same code. *Pedestal* is the output of the ADC with the gate signal applied and without any input signal to any one of its channels. The normalization was needed to adjust all the ADC channels to have the same digital output given the same analog input.

The center of gravity (COG) calculation, at this stage, included the full cluster where COG's are defined by:

$$X_{\text{COG}} = \frac{\sum_{i=1}^n PH_i x_i}{\sum_{i=1}^n PH_i} , \quad Y_{\text{COG}} = \frac{\sum_{i=1}^n PH_i y_i}{\sum_{i=1}^n PH_i} . \quad (6.1)$$

Here n is the cluster length for a given event and PH_i is the pulse height belonging to the corresponding channel. Using the above definitions, we calculated COG's for each clear event. The result of our calculations for the y component of the point 38-2560 which corresponds to $x=8.276$ and $y=4.933$ channels of the PSPMT can be seen as an example in figure 6.4. However, we want to emphasize that in these calculations, we started counting the X and Y channels from zero, not one. Therefore, we have X0 as the first channel and X15 as the last one.

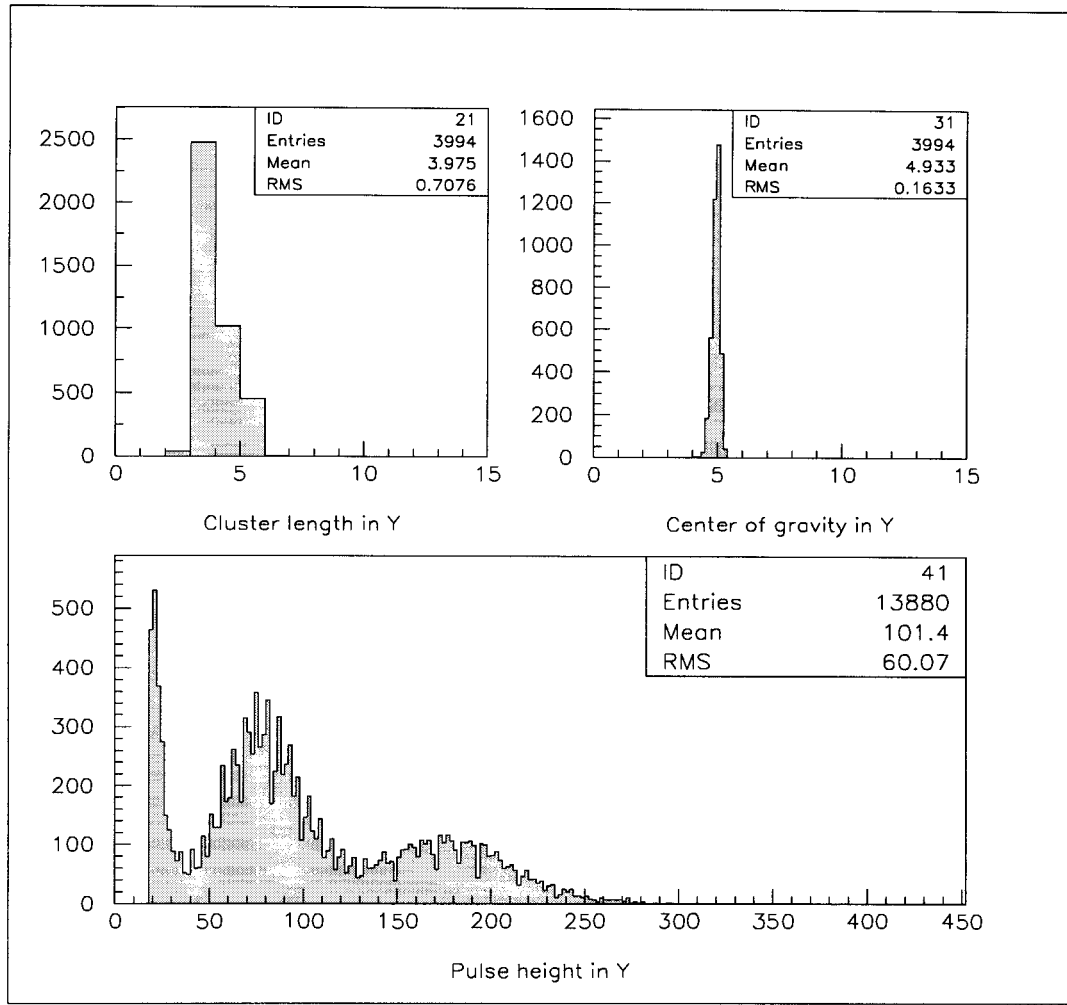


Figure 6.4: A Typical Cluster Length, COG and PH Distributions in Y Direction

In the same figure, we also see the cluster length distribution for the same point. The mean is 3.975 and the maximum is clearly localized at 3. From the PH distribution, one can see the effect of applying a threshold of 20 ADC counts for each event. The peaks in the pulse height distribution may give a clue on the localization. When the LED is on a wire, we get a maximum pulse height on that wire and from the adjacent wires equal pulse heights on the average. However, when the COG of X channels vs COG of corresponding Y channels for all events were plotted, no pattern could be observed and the rms values of the COGs were high. Additionally, X and Y channels showed somehow a small difference in cluster lengths and pulse heights. So we reanalyzed the same data by taking only three channels with biggest pulse heights in the

COG calculation, where the maximum sat in the middle. In this way, we expected to improve our results [44]. So we replace the n 's in formulae 6.1 by 3.

With this new COG calculation, we observed the pattern in COGX vs COGY graph in figure 6.5. Cross checking with the pulse height distributions and individual COG plots, we concluded that the white regions belonged to the regions around the mid-points of the two wires in both directions. On the figure (fig. 6.5), one can notice two things: 1. the misalignment effect that occurred during the scanning process. This effect may be due to the irregularities on the PSPMT shielding cover window; 2. the number of valid events decrease as Y increases. This might be due to a systematic error or the instabilities of the data taking system or the signal generator for the LED. For the scan, we covered an area of $11 \times 18 \text{ mm}^2$ in X and Y. Since the spacing between the wires is 3.86 mm, the number of observed wires agrees with the expected value. This can best be observed in figure 6.6.

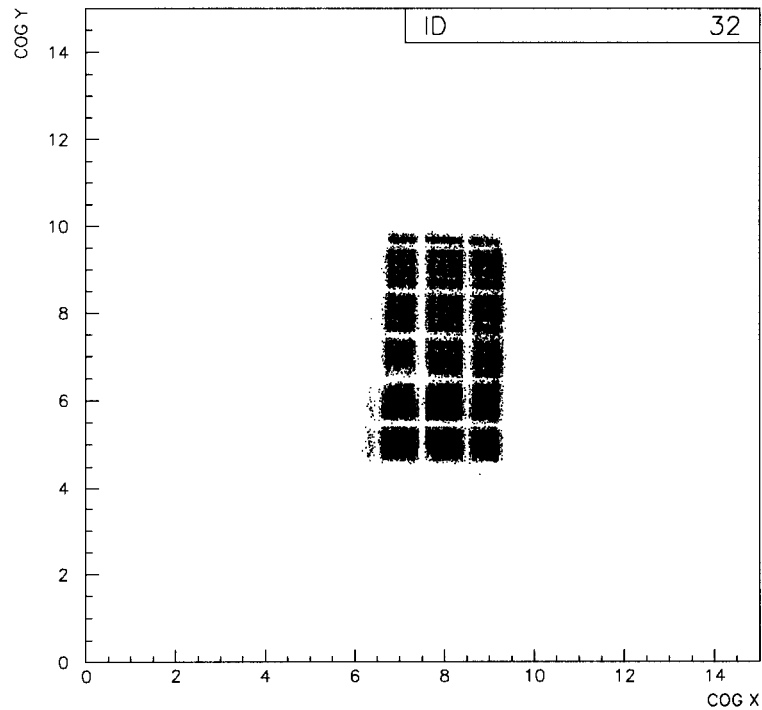


Figure 6.5: COGX vs COGY Graphs Simultaneously Plotted for all Scan Points

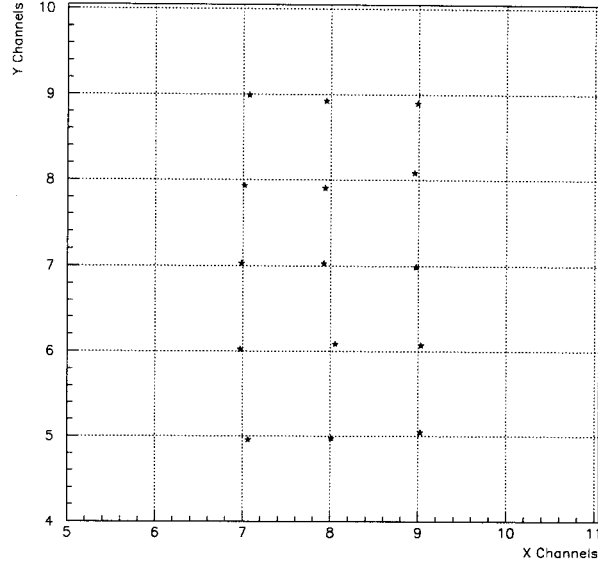


Figure 6.6: COGX vs COGY Values Plotted at the Wire Cross Points

In figure 6.7, we see the COGX graphs for 9 scan points which lie on the 5th Y channel. An overall shift in the COG for this direction can be observed. Numerically, the shift from 38-640 to 38-5120 is $1.96 \pm .12$ channel, which corresponds to a scanning distance of 7.904 mm. The actual wire distance between these points is just 1.96 times the spacing between the wires, which is $7.566 \pm .463$ mm. So this small calculation shows that our result is in an acceptable range.

Finally, we calculated the averages of the pulse heights for each of the three channels contained in the cluster. Using this information and the COG graphs, we tried to determine the position of wires. Since charge-sharing process in cross-wired PMT is a 2-dimensional case concerning both directions at the same time, we chose to estimate the crosstalk at the cross point of X and Y wires. We then chose the points at which we found that the LED is located on the crosses. Out of 15 such points, we chose 10 of them which we thought to be on the cross positions more accurately, thus we will yield in better results. We made two different approaches: first, we wanted to know the average pulse height ratio of the wires adjacent to the wire with the maximum pulse height; secondly, we took the ratio of the same wires to the total pulse height contained in the cluster which is related to the total charge. The results we found are

in table 6.1. We see that the second approach results in smaller standard deviation values for both X, Y separately and for overall channels. One thing to keep in mind is that these results are associated with the crosstalk of our whole detector system.

Table 6.1: Results of Crosstalk Measurements

	% of maximum		% cluster charge	
	Mean	Stdev	Mean	Stdev
X	36.4	6.65	19.4	2.62
Y	31.6	13.0	18.2	5.25
overall	34.0	10.5	18.8	4.14

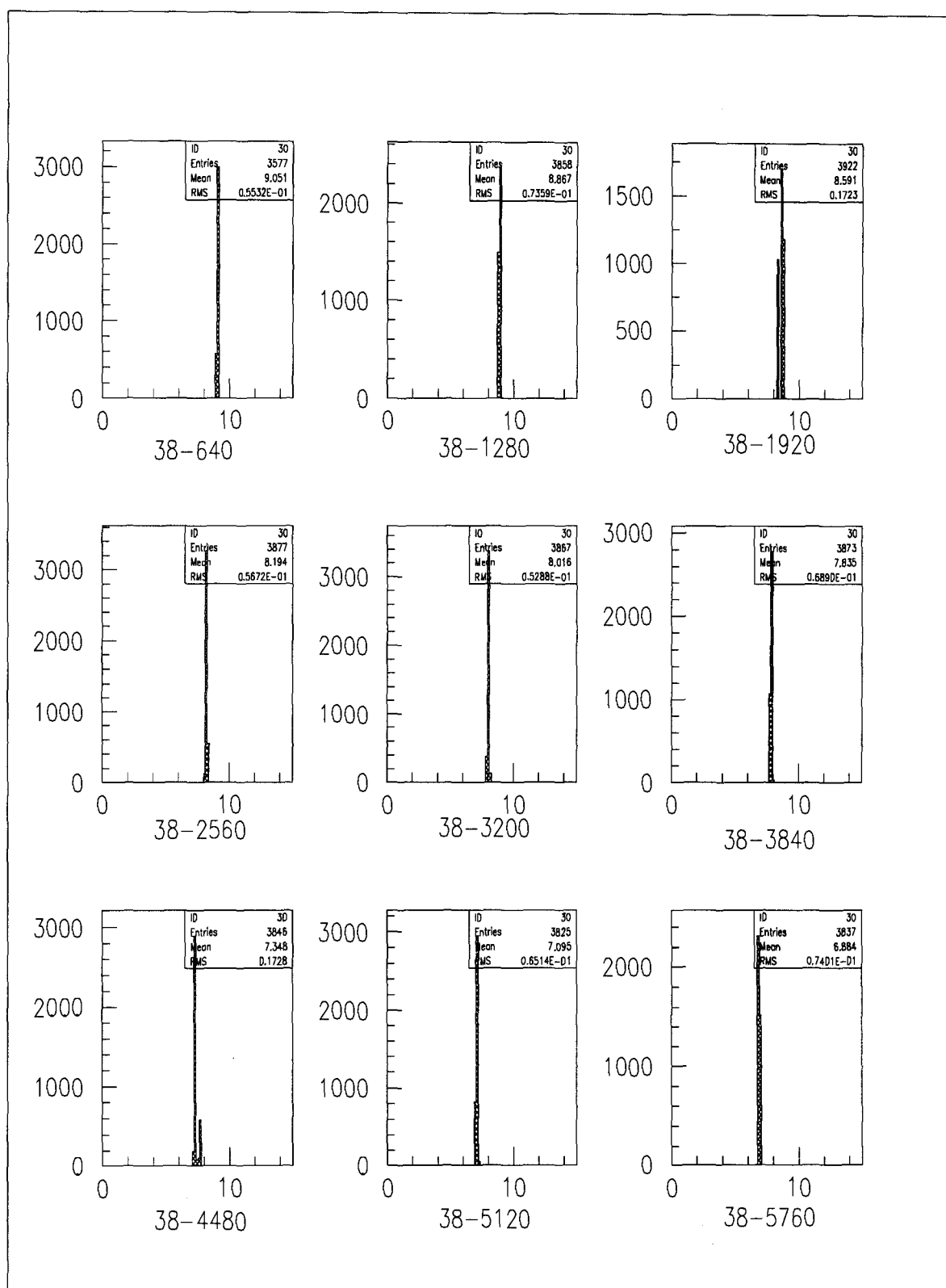


Figure 6.7: COG Plots In X Direction For Point 38

6.3. PET Unit Measurements

6.3.1. Gamma Ray Spectroscopy with CsI(Tl) Crystals

As we mentioned before, inorganic crystal scintillators are suitable to be used when one needs to do spectroscopic analysis. In this study, the gamma ray spectroscopy measurement of CsI(Tl) crystals was performed to determine our detector's energy resolution with two different gamma ray sources. We have also compared the pulse height spectrum of gamma rays obtained by using CsI crystals to those by using plastic scintillators (NE102). A 2x2 matrix of CsI(Tl) crystals (later to be replaced with NE102) was coupled to the single anode PMT (Hamamatsu-R1166). The CsI matrix formed a block which was 30 mm long with a 6x6 mm² square front surface, whereas NE102 formed a block with a length of 40 mm with the same cross sectional area. The crystals and plastic scintillator sticks were each covered by teflon tape. Two different pointlike gamma ray sources were used for the measurements: ¹³⁷Cs ($\tau = 30.2$ years) emits gamma rays with an energy of 0.662 MeV, whereas ⁶⁰Co ($\tau = 5.27$ years) emits gamma rays with energies of 1.333 MeV and 1.173 MeV [45].

The electronic setup of the measurement is given in figure 6.8. In the read-out, the analog signal from the single anode PMT that was coupled to the scintillators was made to self-trigger by passing it through the Fan In/Out unit and sending one duplicate to one of the channels of the 2249W wide channel ADC and the other to the constant fraction discriminator (CFD - ORTEC 935) [46] to set the gate for the ADC and the threshold for the signal⁵. Further delay and gate width adjustments were achieved by using the Dual Timer (CAEN 2255A). The discriminator threshold value and the gate signal were set to get the best peak resolution for the characteristic gamma emission energies of the sources.

⁵the spectra in fig 6.9 were obtained without the preamplifier

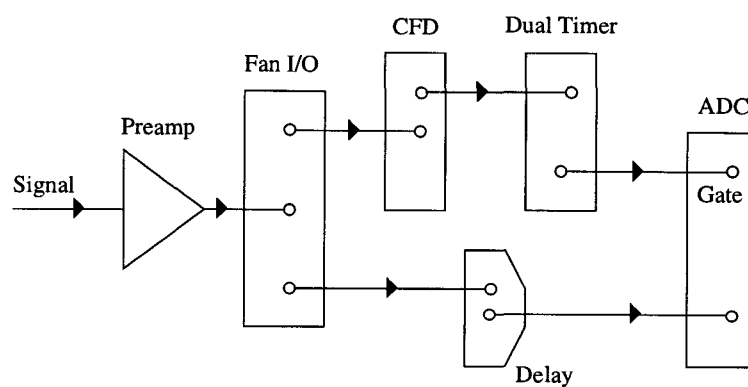


Figure 6.8: The DAQ of the Spectroscopy Measurement

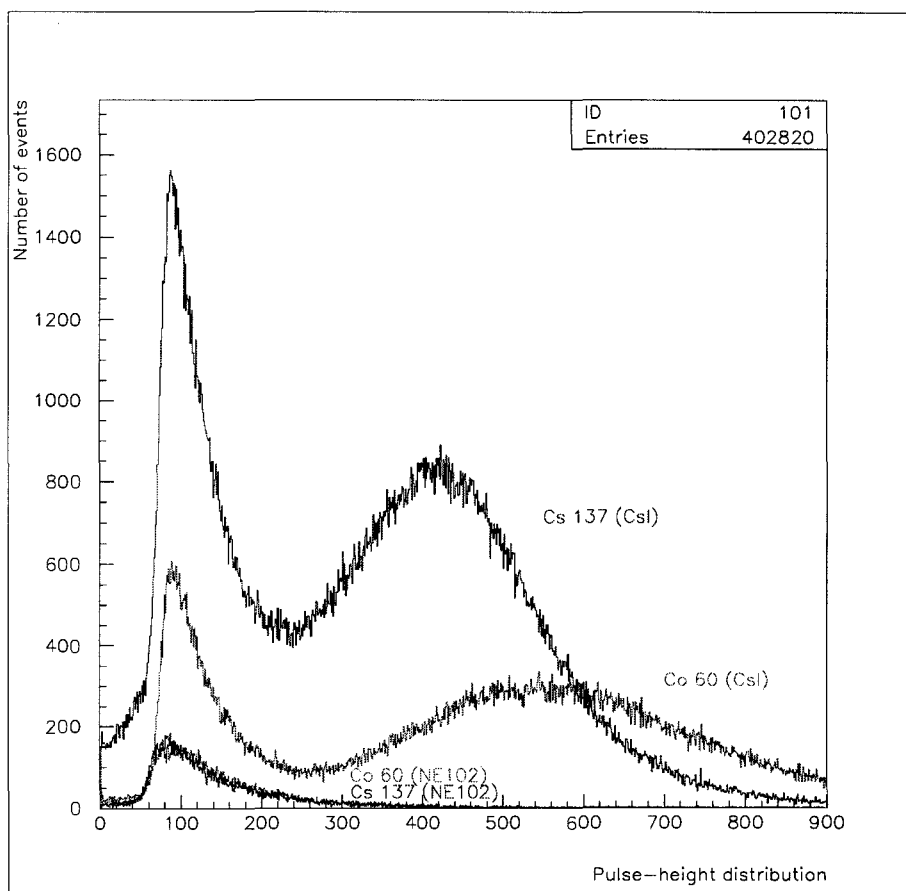


Figure 6.9: Pulse Height Spectra for Different Sources and Scintillators

The resulting pulse height distributions without an amplifier stage is given in figure 6.9. For both scintillators, the discriminator threshold value was set to -63 mV for ^{137}Cs and -116 mV for ^{60}Co during the data-taking. We can resolve two smooth peaks for the sources with CsI(Tl) crystals although they are very wide. On the other hand, we cannot observe any peak with NE102. Furthermore, as can be seen from the figure 6.9, the count rate and pulse heights in this case are lower than the ones for CsI. We, thus, decided to design an amplifier circuitry which may help to enhance resolving the peaks that we obtained with CsI(Tl) and to determine the energy resolution of the detector.

The electronic noise from the system is an important factor to be considered for the energy resolution of the detector. This factor is especially important when the detector is operated in the low energy region (< 1 MeV). If the detector signal is also very weak, it is desired to amplify the signal by a circuitry while avoiding to introduce into the system much of additional noise. The best conventional circuit often used in gamma ray spectroscopy is the charge-sensitive preamplifier. Besides its other advantages [17], its main advantage is that the output voltage is linearly proportional to the charge collected in the detector. A brief description of an equivalent circuit of the detector-charge sensitive preamplifier system can be found in Appendix C.

Another important factor in energy spectroscopy is the pulse-shaping process. The pulse-shaping amplifier has several functions such as amplifying the signal to optimize the energy resolution and minimizing the pile-up effect which arises from the overlap of two successive pulses. This overlap causes distortion in the energy spectrum of the detector. It is preferred that the pulse-shaping results generally in a Gaussian form. A commonly used technique is CR-RC shaping or a cascade of these stages [16]. The drawback of such a circuit is the presence of an undershoot in the shaped pulse. This leads to a deterioration of the amplitude of the next coming pulse if it starts in this negative tail region of the previous pulse. To solve this problem, another special technique, pole-zero cancellation may be used. It is useful to remark that, extraction of the energy information requires long pulse width from the amplifier (to collect all the charge from detector), but to work with high counting rates and to keep time informa-

tion, short pulse widths are favoured. So, if both informations are needed, a reasonable compromise must be made.

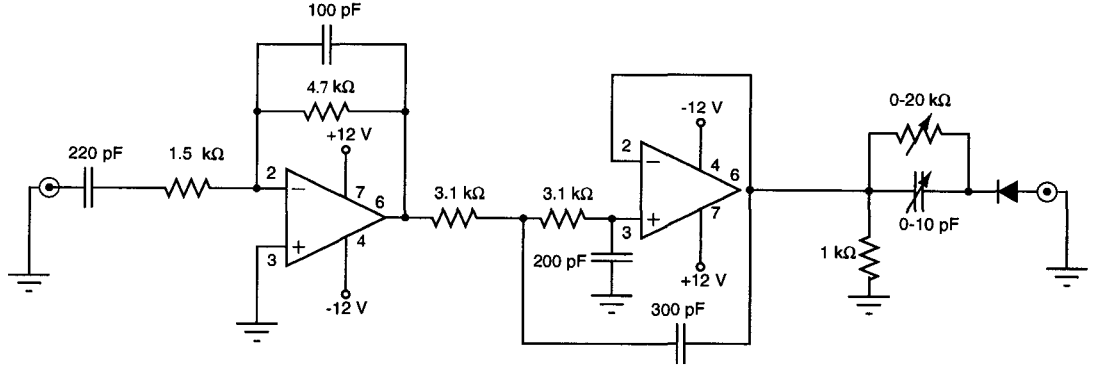


Figure 6.10: Preamplifier for Enhancing the Resolution of the Energy Peaks

The circuit configuration of the amplifier system used in our setup is seen in figure 6.10. The topology of the amplifier is somewhat similar to the one described in [47]. It's a three stage amplifier: the first stage (integration stage) is the charge-sensitive preamplifier; the second is pulse-shaping stage and the third stage is in charge of pole-zero cancellation. The integration stage of our charge-sensitive preamplifier is based on the fast and low-noise video operational amplifier (AD 829JN, Analog Devices). It was chosen because of its high bandwidth (120 MHz) and low input voltage noise ($1.7 \text{ nV}/\sqrt{\text{Hz}}$). The signal-shaping circuit is a nearly gaussian CR-RC² type [48]. The shaping time of the circuit was measured to be $1.5 \mu\text{s}$ to minimize electronic noise and pile-up effects. The pole-zero cancellation stage has been designed using traditional trimmer adjustments.

Energy Resolution: The detector *energy resolution* is defined to be the ratio of the width of the peak distribution at the level of one half of the maximum pulse height (FWHM) to the maximum pulse height itself (PH_0). In mathematical formulation, one can write:

$$R = \frac{FWHM}{\text{PH}_0} \times 100 \quad (6.2)$$

where R is just a dimensionless ratio usually expressed as a percentage.

In general, this distribution is in the form of a Gaussian shape, thus, a Gaussian curve can be fitted to the peak which automatically sets the FWHM value to 2.35 times of the variance of the distribution. The pulse height distributions and the Gaussian fits for both of the sources can be observed in figure 6.11. The spectra are obtained with CsI and with the discriminator treshold settings as: -91 mV for ^{137}Cs and -196 mV for ^{60}Co .

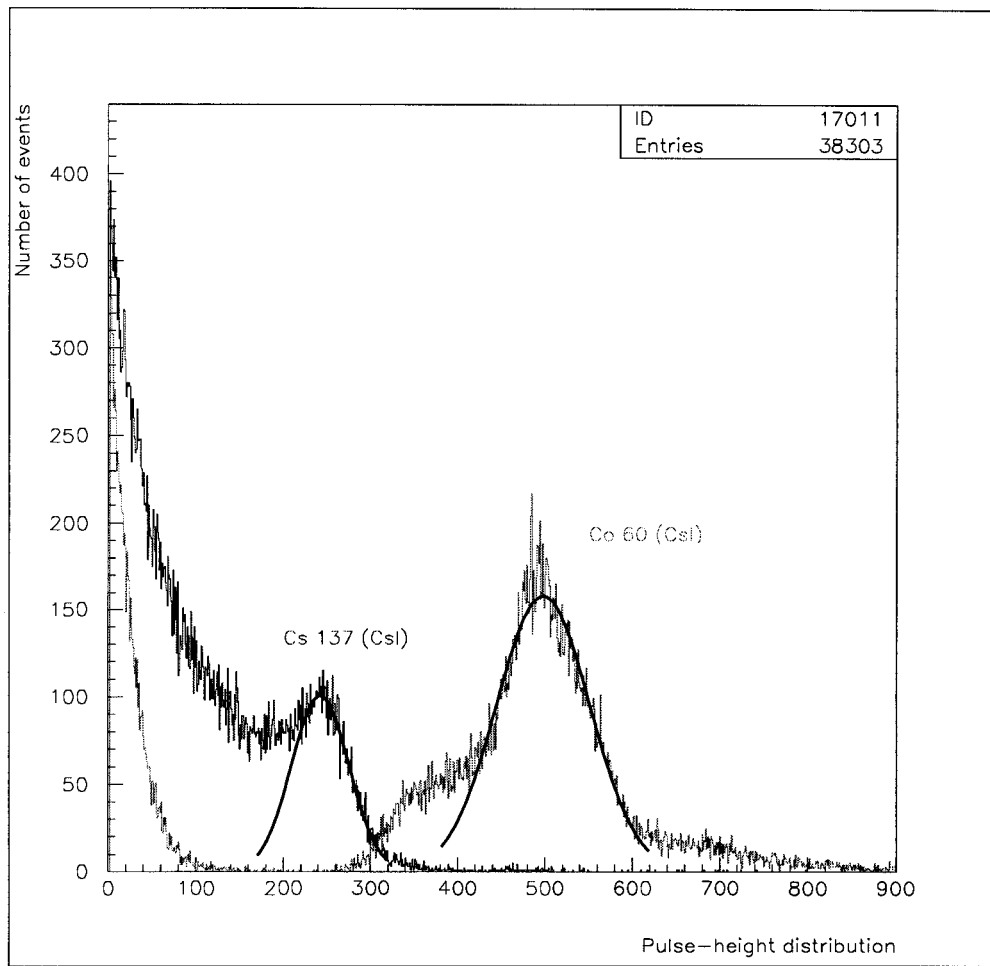


Figure 6.11: Pulse Height Spectra After the Preamplifier

Table 6.2 lists the results of the fitted Gaussians for both gamma sources and calculated FWHM's and resolutions. The results for ^{137}Cs showed that it's not quite possible to resolve yet the two energies of ^{60}Co , therefore we fitted the whole peak for ^{60}Co .

It's not misleading that the resolutions found for ^{137}Cs and ^{60}Co are different since the resolution of the detector is dependent on the energy of the source by its inverse square root [16]. Thus, the resolution of ^{137}Cs is expected to be about 1.30 times the one that of ^{60}Co for the 1.173 spectrum of ^{60}Co . The results we found are in good agreement with this ratio, since, for our case, it turns out to be 1.28.

Table 6.2: Results of Gaussian Fits and Energy Resolutions

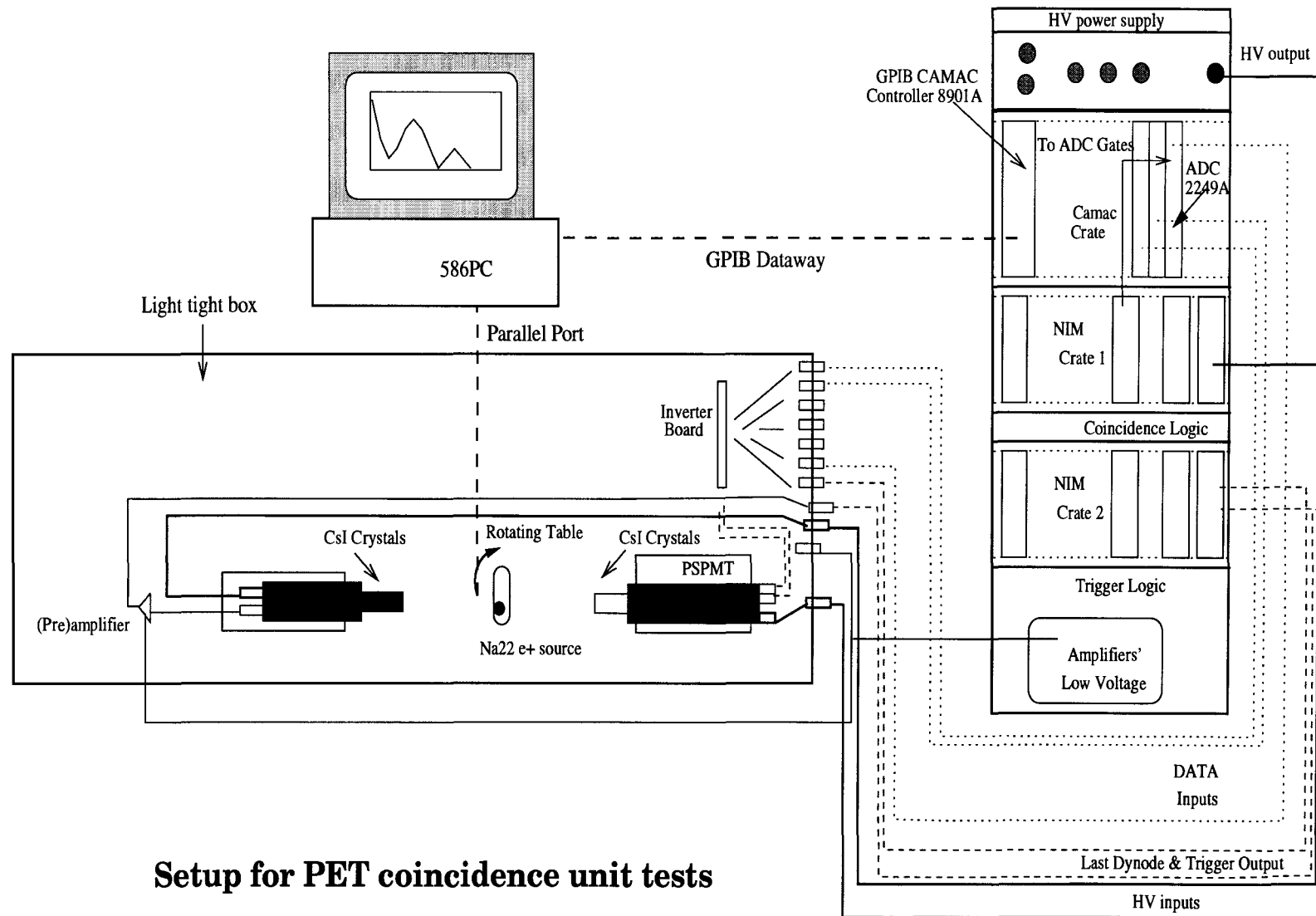
	Amplitude	PH_0	σ	FWHM (2.35σ)	R (%)
^{137}Cs	100.48 ± 1.63	242.34 ± 1.12	32.88 ± 1.02	77.27 ± 2.40	32.0 ± 1.0
^{60}Co	157.85 ± 1.55	497.82 ± 0.51	53.24 ± 0.56	125.11 ± 1.32	25.1 ± 0.3

6.3.2. Measurements with PET Unit and Image Reconstruction

As we have mentioned before, 2-D image reconstruction of a slice of the human body with positron emitters is usually done by using a ring of individual detectors. This is a need for the radiation health and time consumption problem. In principle, the aim is to get tracer distribution information from different angles. In that manner, only one pair of detectors in coincidence is enough when one rotates it around the distribution. For our case, due to the limitations imposed by the light tight box in which the detector unit is located, we rotated the source instead. This we can easily do when the source is located off the axis passing through the center of the plane of view of the PMT's. Usually, both of the coincident detectors are PSPMT's in PET. However, we had one PSPMT and one single anode PMT which we call the trigger PMT (EMI 9839A).

The experimental setup used for the coincidence measurement is shown in figure 6.12. The PMT's are face-to-face with the encapsulated point-like ^{22}Na positron source in between them. The distance between the two PMT's is 19 cm which defines the diameter of the plane of view of the system.

Figure 6.12: Schematic View of the PET Coincidence System Setup



The source capsule served as the target material since positrons emitted from ^{22}Na has an endpoint energy of 545 keV and even with that energy the positrons easily annihilate within the plastic encapsulation material. The dimensions of the source capsule is 23x2x11 mm. However, at each angle, we positioned the capsule such that the plane defined by the thickness times the length of the capsule (23x2 mm) was parallel to the surfaces of the PMTs. This confines the positrons in an approximate sphere of 1 mm radius.

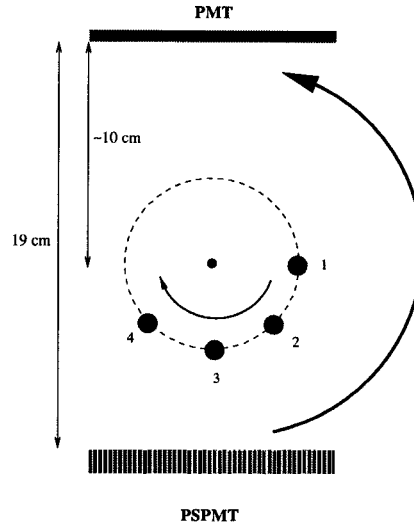


Figure 6.13: Rotation Directions for Data-taking

The initial position of the source can be seen in figure 6.13. It was located at this first measurement at $(1.2 \pm 0.1, 0.4 \pm 0.1)$ cm, closer to the PSPMT, if we assign the center to be the midpoint of the two detectors. This first measurement angle was assigned to be the $\theta = 0$ degrees. From three more points, namely at 45, 90 and 135 degrees which are numbered accordingly in figure 6.13, we registered 1-D projections obtained by reading the outputs of the PSPMT channels coupled to 2x8 crystal matrix. In these measurements we required the time coincidence of the signals obtained from PSPMT and trigger PMT.

The coincidence setup of the two detectors is given in figure 6.14. After compensating the relative delay of the outputs of both PMT's, the anode output of the trigger

PMT and the last dynode signal of the PSPMT are send to the discriminator (CFD) unit in order to eliminate the noise and to obtain a NIM level signal. We then implemented the AND logic between these two signals using a coincidence unit with a time window of 10 ns. The three outputs of the coincidence unit are used to open the gates, through a discriminator, of the three ADC modules (LeCroy 2249A) which read the 32 anode wires of the PSPMT.

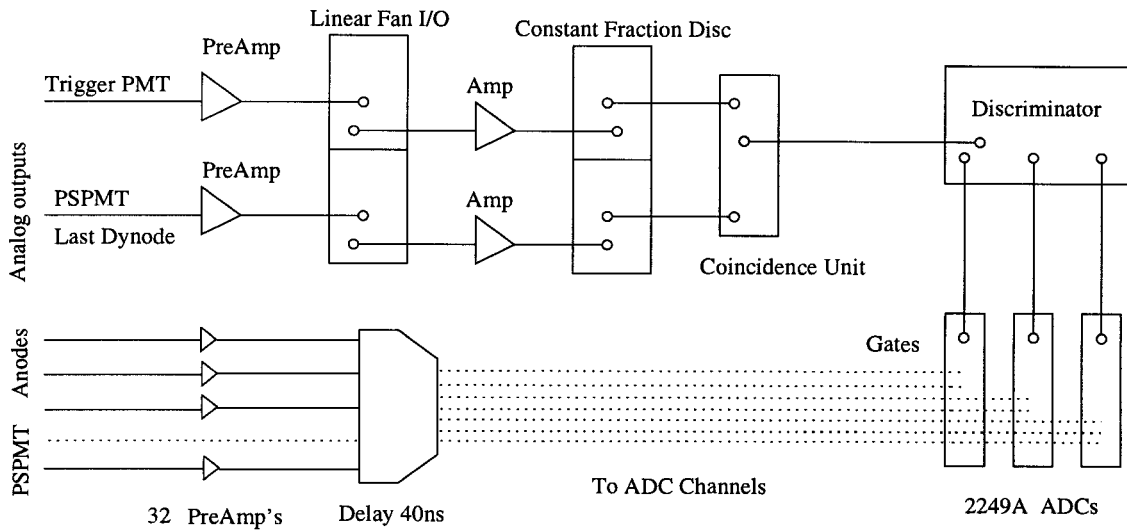


Figure 6.14: The DAQ Setup of the Coincidence Measurement

In order to properly extract the useful information from the ADC readout, we analyzed this data using a slightly modified version of the code used in crosstalk measurements. The modifications were in the algorithm to find the clusters and to calculate the center of gravities. By observing the raw data we have noticed that the noise signals were consisting of clusters of length three and less whereas the real signal clusters were of length four and above. We also implemented an upper level cut to the data to eliminate the high pulse heights which were probably originated from the energetic gammas (of 1.274 MeV) emitted by the daughter nucleus during the positron decay process. One can see the calculated the COG's from the data taken at each of the four positions in figure 6.15.

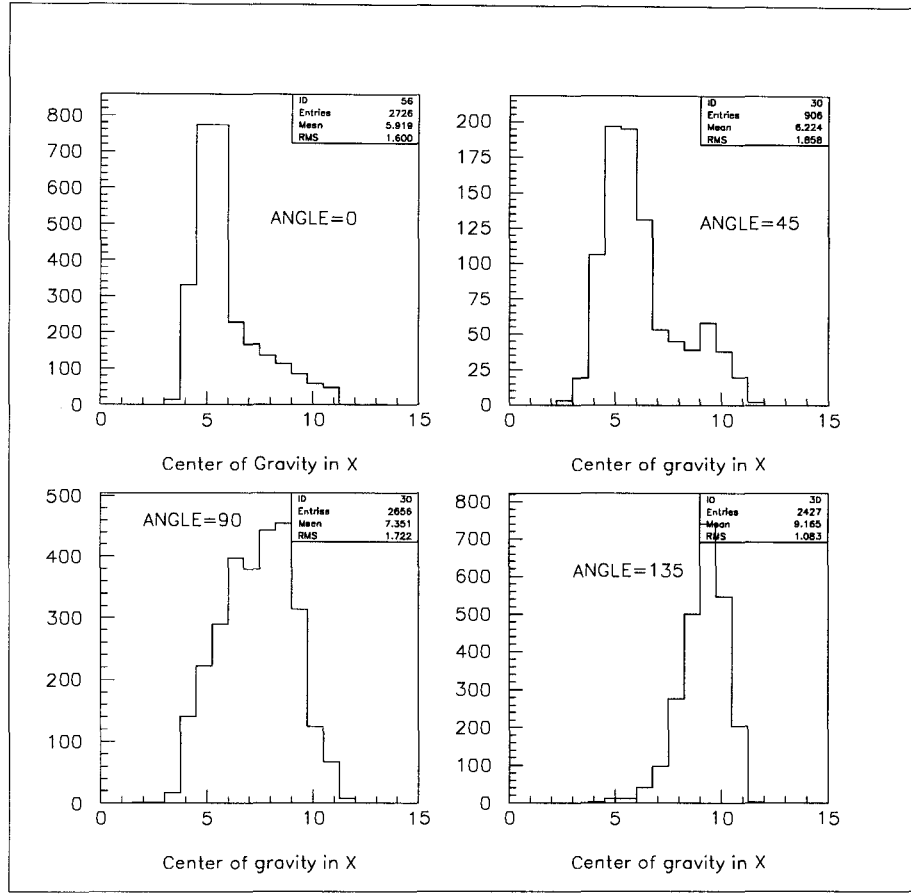


Figure 6.15: COG Plots for Different Detector Angles

The idea in the PET image reconstruction is to backproject the 1-D images obtained in the COG histograms to a square matrix of the size of the plane of view. This back-projection consists of the summation of the number of counts in each COG histogram bin which also defines the measurement unit in the reconstruction. Since each 1-D histogram is taken at a specific angle, we have the number of counts and the viewing angle informations, i.e., projection data, for each point ($P(\text{COG}, \theta)$) which can be utilized to reconstruct the original image in cartesian coordinates according to the formula [12]:

$$f_{\text{back}}(x, y) = \frac{\pi}{M} \sum_{j=0}^{M-1} P\left(x \cos\left(\frac{\pi j}{M}\right) + y \sin\left(\frac{\pi j}{M}\right), \theta_j\right) \quad (6.3)$$

where M is the number of measurement angles which is four in our case. For the localization measurement in the 2-D plane that we represent by the $(x - y)$ coordinates, we

used the following convention: Since we have a total of 16 wires separated by 3.86 mm the total length seen by the PSPMT is about 61.2 mm . Remembering that our scintillator sticks are 3 mm wide which also determines our uncertainty in the measurement, we have a natural binning of the 2-D plane as 20x20. Thus in equation 6.3 the (x, y) coordinates are from 1 to 20. Let us note here that the values of x and y are only for naming, they do not stand for absolute coordinate measurement. To implement this reconstruction algorithm, we have written a small Fortran code which can be found in Appendix E. The result we have found for the position of the source is $(0.9 \pm 0.3, 0.5 \pm 0.3)$ cm. In figure 6.16, we show the figure which gives the localization of our pointlike source in the 2-D plane in a good agreement with the actual position.

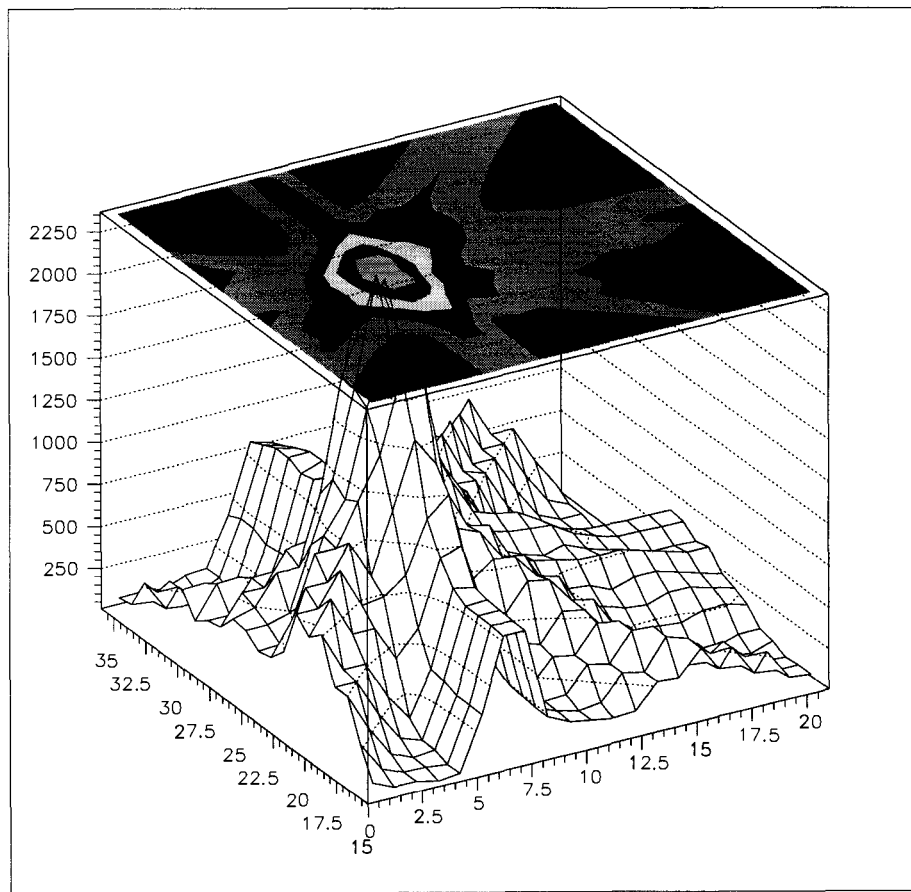


Figure 6.16: 3-D and 2-D Representations of the Reconstructed Image

7. CONCLUSION

In this work, we have tried to apply some basic principles of experimental particle physics and detector physics to some other areas such as medical imaging and radiotherapy.

The crosstalk measurement, which served as a test for our setup, gave us the idea that the cross wired PSPMT's can be utilized in PET imaging. We got a relatively high crosstalk ($\approx 35\%$) in maximum pulseheight channel to its nearest neighbor comparison. However, we have also shown that the proper application of the center of gravity algorithm can yield accurate results.

In the CsI(Tl) scintillator stick test measurements, we familiarized with this new material and we have observed the necessity to produce a preamplifier for pulse shaping. While doing the spectroscopic analysis, we have calculated the energy resolution of our system with CsI(Tl) crystals with the results which are acceptable for a system like ours.

Based on these conclusions, and on the simulation results, we have decided that we could reconstruct a 2-D image of a point like object using PET techniques. We then performed the experiment and we got a very satisfactory 2-D PET image. This setup can be enhanced to get better results. These enhancements include the utilization of a faster and better scintillator crystal type, of two face-to-face PSPMTs, and an improved reconstruction technique which should also include filtering algorithms [12].

Appendix A

Proton Therapy Simulation with GEANT

Medical imaging is not the only application of radiation physics to medicine. In this small section, we want to briefly discuss how the energy loss of particles can be utilized as a therapy tool for oncological treatments. Conventionally, X-rays and electron beams have been in use for this purpose for years, but fast charged heavy particles such as protons and alphas are becoming more popular for the reasons that we will mention below.

Radiobiologically, the effect of radiation is directly proportional to its ion creation power in the tissue as it is also dependent on the type of the tissue in consideration [49]. Therefore, the particle damages any cell biologically as long as it can stay in the vicinity of the cell to produce necessary number of ions as it passes by. Thus, in radiotherapy, the aim is to externally irradiate a tumor inside the body by an optimal dose of ionizing radiation, thus destroying it, while also avoiding the damage to the healthy cells in the neighborhood. In this manner, X-rays and electron radiotherapy have one thing in common: they are not ideally good at targeting the tumor hidden deep inside the body both space-wise and dosage-wise. Space-wise: they highly scatter before reaching the tumor. Electrons, being light charged particles, encounter multiple scattering; photons encounter compton scattering, which diverges them from the beam direction drastically. Dosage-wise: the ionization for electrons is high on small penetration depth, thus yielding the result of damaging normal tissue upstream rather than the tumor, and similarly for photons, interaction may take place between the photons and the medium long before reaching the target tumor which again gives the similar result as that of the electron. On the other hand, proton, with its mass about 2000 times greater than that of the electron ($m_p = 938 \text{ MeV}$), can fulfill the requirements of targeting the deeply-seated tumor. In fact, it has long been thought that proton is suitable for such a treatment [50] but the utilization came later when accelerators with higher energy have been introduced to the field. To have an idea of the relative dose introduced to the tissue by different radiation types, one can observe figure 7.1.

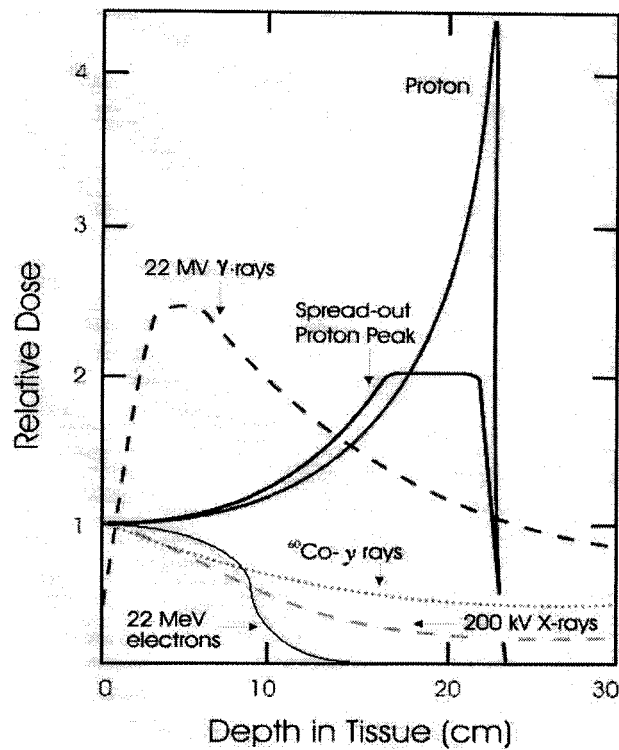


Figure 7.1: Comparison of Different Radiation Types Currently Used in Radiation Therapy [51]

The key concept for proton cancer therapy is the *Bragg Peak* which was already mentioned in chapter 2 of this work. A sufficiently energetic proton (kinetic energy > 20 MeV) enters the body, moving nearly in the velocity range $1/3c - 1/2c$, c being the velocity of light, and it starts a continuous energy loss due to ionization. As it slows down, it deposits more energy per distance traversed. Thus, the number of ions generated per unit volume of tissue increases as it reaches the target. At the distance corresponding to the Bragg Peak, where it reaches the maximum ionization dosage, the proton slows down to nearly 10 MeV. After that point, the ionization stops because now the proton starts absorbing electrons from the medium. In addition, on the average, the proton undergoes multiple scattering less and is not deflected much from its trajectory.

To illustrate how the Bragg Peak can be used to tune the proton's energy according to the desired depth in the tissue, a simulation was performed using the GEANT pack-

age. It's important to note that GEANT cannot simulate hadronic processes below 10 MeV. In our case, this does not cause a problem because it's known that with energies below 10 MeV, the proton already stops ionizing.

For the simulation, an average human body is created using the standard (but limited) shapes of GEANT. We specified two mediums for this body, which we called soft tissue ($d_{soft}=0.987 \text{ gr/cm}^3$) and bone tissue ($d_{bone}=1.486 \text{ gr/cm}^3$). The elemental components of these materials together with their density is similar to those of the MIRD-5 phantom [52]. We located the body at the origin of our GEANT universe (MARS) and the protons were directed to the body at a distance $x=-100.0 \text{ cm}$ and perpendicular to the y - z plane at $z=-5.0 \text{ cm}$. This corresponded to the abdomen region of the body. The energy loss of the protons in air at such a distance was negligibly small (a few tens of keV) so no corrections to the kinetic energy were needed to be made.

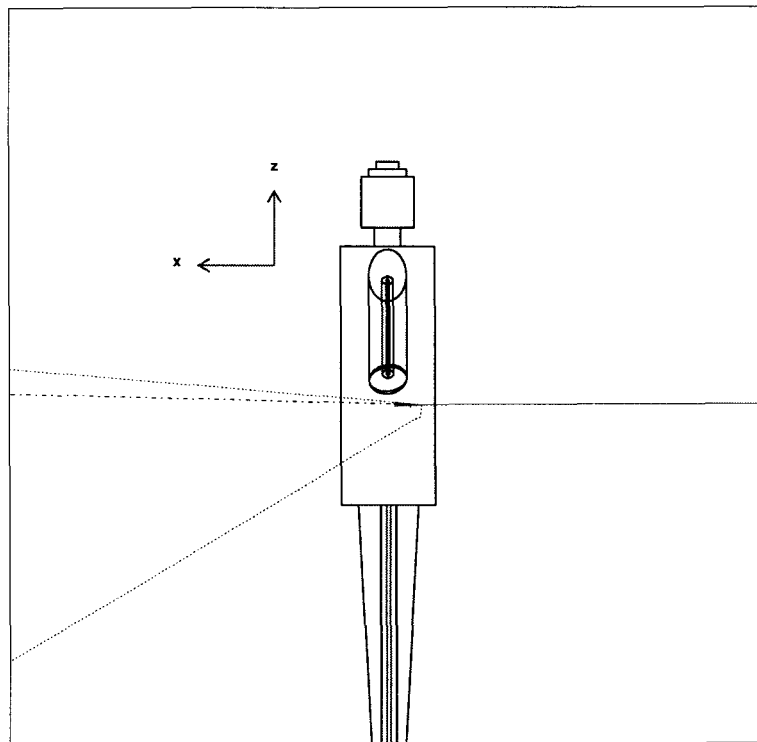


Figure 7.2: Human Body Viewed from the Projection on X-Z Plane.

The body representative and tracing of a few events are seen in figure 7.2. Please

note that the arms are open sideways. Proton tracks are represented with a red line and secondaries produced during tracking such as gammas and alpha particles are observed as well.

For 15 different initial proton energy values, ranging from 40 MeV to 180 MeV, the specific energy loss was plotted as a function of the range in the tissue. From these plots, the Bragg Peak point was obtained to get the curve which relates the initial proton kinetic energy to its range. For each of the plots, the data was fitted to a curve given as:

$$y = A/\sqrt{B - x} \quad (7.1)$$

since it's known that the specific energy loss of heavy particles is proportional to its range with such a relation [16]. Experimentally, this curve yields the Bragg Peak about the point where the asymptotic behaviour has been reached due to the fact that it no longer ionizes particles above that point. The maximum range of the proton is taken as the value of the asymptote which is determined by the parameter B in the equation. Parameter A helps to correct the small x values.

For the dE/dx versus x curve in figure 7.3 which is for 100 MeV protons, the points that don't fit the general behaviour of the curve are due to the protons that have encountered scattering along their way to the target. The error bars indicate that the number of occurrences of such events are small. This shows that the scattering of protons is not much just as we expected it to be. We also took notice of other possible interactions that can yield secondary particles. The percentage of such interactions in each run is also calculated to have a rough idea. The results obtained show that the hadronic interactions take place in the body for nearly 4 % of the total events for the low energies that we considered, whereas, for the high values it can reach up to 20 %. From these interactions, α particles which may be a danger for the patient under therapy can be produced.

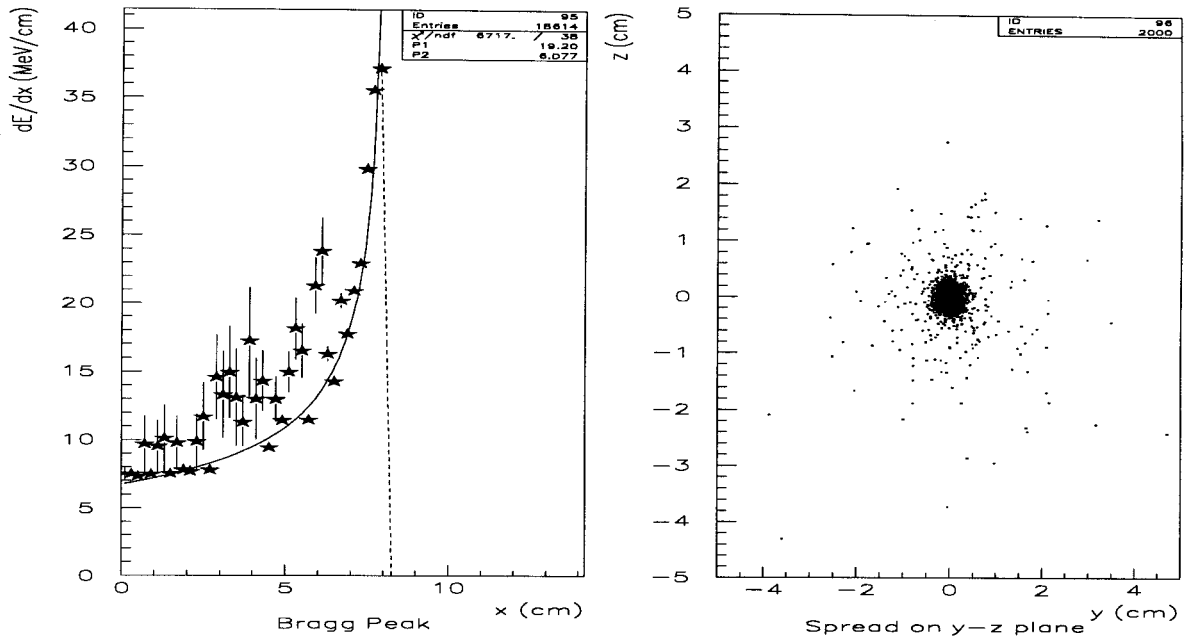


Figure 7.3: Bragg Peak Curve and Spread of Protons from Initial Direction for 100 MeV Protons

Also we have plotted the spread of protons from the initial direction for all initial proton energies (fig. 7.3). To estimate how the proton deviates from its trajectory on the average is necessary from the point of view that it's important to know how large an area can be treated with such conditions. The average range of protons in the plane perpendicular to the beam direction can be found in the table at the end of the section (table 7.1). In this calculation scattered protons were taken into account as well. One can see that a proton remains in its initial direction approximately within a centimeter for the 100 MeV protons.

We have also simulated when the beam crossed bone tissue. We targeted one leg of the body and arranged the proton energy so that it will stop after passing the bone. We could obtain the Bragg Peak successfully.

The table of maximum range corresponding to the initial proton kinetic energy is given in table 7.1. When plotted, these yield the curve in figure 7.4 which we fitted to

a function expressed as [16]:

$$y = Ax^B \quad (7.2)$$

where A is found to be 31.31 and B to be 0.58. This is now the curve that we have found to relate the initial proton energy to the range in human soft tissue.

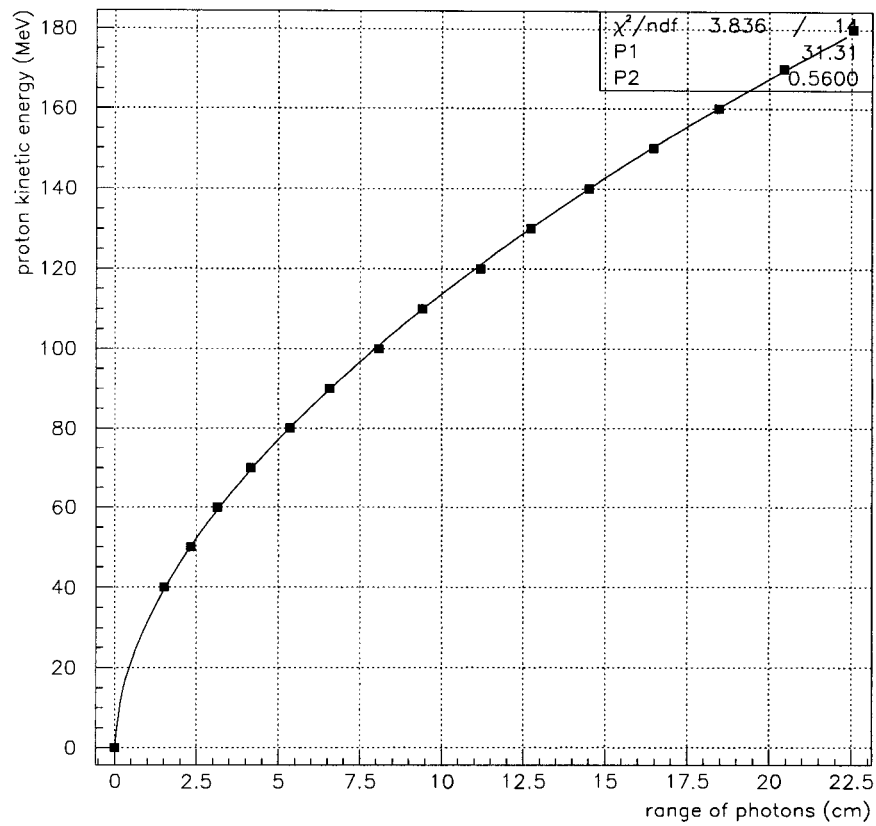


Figure 7.4: Graph Showing the Dependence of Proton Energy to Range in Soft Tissue. Curve is fitted to equation 7.2

Table 7.1: Table of Obtained Values for Different Proton Energies

T_p (MeV)	Range (cm)	R_{spread} (cm)
40	1.512	0.06
50	2.317	0.08
60	3.129	0.10
70	4.156	0.15
80	5.358	0.19
90	6.576	0.23
100	8.077	0.30
110	9.407	0.34
120	11.20	0.41
130	12.72	0.44
140	14.50	0.50
150	16.47	0.53
160	18.46	0.60
170	20.45	0.62
180	22.56	0.66

Appendix B

Simplified Program FlowChart for GEANT

MAIN	user routine
GZEBRA	initialization of ZEBRA system, dynamic core allocation
UGINIT	user routine
GINIT	initialization of GEANT variables
GFFGO	interpretation of data records
GZINIT	initialization of ZEBRA core divisions and link areas
GPART/GSPART	creation of the particle data structure JPART
GMATE/GSMATE	creation of the material data structure JMATE
user code	description of the geometrical setup, of the sensitive detectors, creation of data structures JVOLUM, JTMED, JROTM, JSETS
GPHYSI	preparation of cross-section and energy-loss tables for all used materials
GRUN	loop over events
GTRIGI	initialization for event processing
GTRIG	event processing
GUKINE	(user) generation (or input) of event initial kinematics
GUTREV	(user)
GTREVE	loop over tracks, including any secondaries generated
GUTRAK	(user)
GTRACK	control tracking of current track
GFINDS	find current volume in the geometry tree
GUSTEP	(user) recording of hits in data structure JHITS and of space points in data structure JXYZ
GUPARA	called if the particle falls below the tracking threshold
GTGAMA/GTELEC/...	tracking of particle according to type
GFSTAT	fill banks for volume statistics
GSTRAC	store information of the current track segment
GUSTEP	(user) recording of hits in data structure JHITS and of space points in data structure JXYZ
GTMEDI	finds in which volume/medium the current space point is
GUSTEP	(user) recording of hits in data structure JHITS and of space points in data structure JXYZ
GUDIGI	computation of digitisations and recording in data structure JDIGI
GUOUT	output of current event
GTRIGC	clearing of memory for next event
UGLAST	(user)
GLAST	standard GEANT termination

Appendix C

List of Processes Involved in GEANT

1. Processes involving the photon:
 - (electron,positron) pair conversion
 - Compton collision
 - Photoelectric effect
 - Photo fission of heavy elements
 - Rayleigh effect
2. Processes involving electron/positron:
 - Multiple scattering
 - Ionisation and delta-rays production
 - Bremsstrahlung
 - Annihilation of positron
 - Generation of Cherenkov light
3. Processes involving muon(+,-):
 - Decay in flight
 - Multiple scattering
 - Ionisation and delta-rays production
 - Ionisation by heavy ions
 - Bremsstrahlung
 - Direct (electron,positron) pair production
 - Nuclear interaction
 - Generation of Cherenkov light
4. Processes involving hadrons:
 - Decay in flight
 - Multiple scattering
 - Ionisation and delta-rays production
 - Hadronic interactions

Appendix D

Charge-sensitive Amplifiers

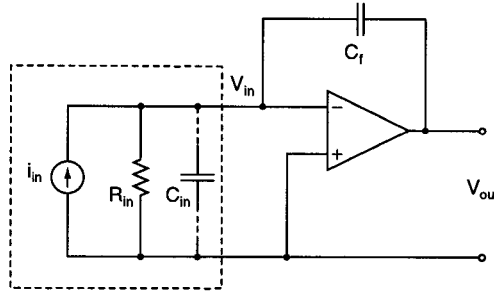


Figure 7.5: Equivalent circuit of the detector-amplifier system

In this figure, i_{in} is the current from the detector, C_{in} is the capacitance of the detector and C_f is the feedback capacitance used in the amplification circuit.

$$V_{out} = -A \frac{V_{in} C_{in}}{C_f} = -A \frac{Q_{in}}{C_f} \quad (7.3)$$

where A is the gain of the amplifier, Q_{in} is the charge on the input capacitance of the detector. This relation states that the amplitude of the output voltage is proportional to the charge which is collected in the detector and is related to the energy deposited by the incident particle. Charge drawn on C_f will produce an output voltage which may stay indefinitely on it, so we can discharge it at the appropriate time by placing a resistor (usually a large one) across the feedback capacitance.

Appendix E

Source Codes of Programs Used

1. Crosstalk Analysis Program

```

/*****
*                               muge.c                               *
*               written by Muge Karagoz (MGU)   03/98               *
*               binary file reading imported from genel.c         *
*               (thanx to NGU)                                     *
*****/
#include <stdio.h>
#include <stdlib.h>
#include <fcntl.h>
#include <math.h>
#include <f2c.h>

#define MAXMOD 32

/* this is absolute need for our system */
struct{
    float a[2000000];
}pawc_;
#define pawc_1 pawc_

/* this is to fake the f2c translator */
int MAIN__ ( ){ };

int main(int argc, char *argv[])
{
    /* cernlib functions */
    extern int hrput_(),hbook1_(),hf1_(),hfill_(),hf2_(),hlimit_();
    extern int hbprof_(),hpak_();
    extern int maxrze_();

    /* variables for hbook stuff */
    int hlim=500000,fzero=0,izero=0;
    float weight=1.,tmp;
    int min_ch,max_ch,num_ch;
    int h_cl_mult_x=10, h_cl_mult_y=11;
    int h_cl_len_x=20, h_cl_len_y=21;
    int h_cog_x=30, h_cog_y=31, h_cogx_vs_cogy=32;
    int h_ph_x=40, h_ph_y=41;

    /* variables for binary file reading */
    int ifp,N,tty,max_mod,n[MAXMOD];
    int chnum[MAXMOD],ch_a[128][MAXMOD];
    int day,month,year,dummy,i,j,k,cur_mod,a,curmod,no,size,size2=0;
    char name[32];

    /* variables for analysis */
    float data[2][16],normcoef[2][16];
    int curr_channel,ldat[2],ii,jj,mm,valid=0;
    int clus_start[2], clus_len[2],clus_num[2], cl_max_pos,dump[2];
    int ngu;
    float clus_min=20.;
    float maxdat=1000.,mindat=3.;
    float ph_sum[2],ch_sum[2],ph_ave_sum[2][16],ph_ave[2][16],data_sum[3];
    float cog[2], ka=0.00, b[2],temp[16],ce[2][3],cog_count;
    float sum_n[2][3],sum_n2[2][3],cog_stdev[2][3],cog_ave[2][3];

```

```

if (argc != 4) {
    printf("\n%s%s%s%s\n", "Usage: ", argv[0], " binary_file_to_read",
        " 2/1/0tty", " hst_file_name");
    exit(1);
}

/* hbooking stuff */
hlimit_(&hlim);
min_ch=0,max_ch=10,num_ch=10;
hbook1_(&h_cl_mult_x,"Cluster multiplicity in X",
    &num_ch,&min_ch,&max_ch,&fzero,25L);
hbook1_(&h_cl_mult_y,"Cluster multiplicity in Y",
    &num_ch,&min_ch,&max_ch,&fzero,25L);
min_ch=0,max_ch=15,num_ch=15;
hbook1_(&h_cl_len_x,"Cluster length in X",&num_ch,&min_ch,&max_ch,&fzero,19L);
hbook1_(&h_cl_len_y,"Cluster length in Y",&num_ch,&min_ch,&max_ch,&fzero,19L);
min_ch=0.,max_ch=15.,num_ch=100;
hbook1_(&h_cog_x,"Center of gravity in X",&num_ch,&min_ch,&max_ch,&fzero,22L);
hbook1_(&h_cog_y,"Center of gravity in Y",&num_ch,&min_ch,&max_ch,&fzero,22L);
min_ch=0.,max_ch=500.,num_ch=250;
hbook1_(&h_ph_x,"Pulse height in X",&num_ch,&min_ch,&max_ch,&fzero,17L);
hbook1_(&h_ph_y,"Pulse height in Y",&num_ch,&min_ch,&max_ch,&fzero,17L);

min_ch=0.0,max_ch=15.0,num_ch=200;
hbook2_(&h_cogx_vs_cogy,"COG X vs COG Y",
    &num_ch,&min_ch,&max_ch,&num_ch,&min_ch,&max_ch,&fzero,15L);

tty=atoi(argv[2]);

/* N= NUMBER of READINGS
   tty= Do we want reporting?
   do_hbook= Do we want histo package?
   max_mod= Number of modules
   n[]= the array which contains the slot numbers
   num_bits[]= the resolution of each module
   hist_ch_num[]= Channel number for histogram for each module
   chnum[]= the array to give the max number of channels to read
   */

/* initializing average ph values */

for (i=0;i<=1; i++) for (j=0; j<=15; j++) ph_ave[i][j]=0.0;

/* determination of norm coefs for the ADC channels used */
/* for (i=0;i<=1; i++) for (j=0; j<=15; j++) normcoef[i][j]=1.0; */
normcoef[0][0]=1.171; normcoef[0][1]=1.156;
normcoef[0][2]=1.162; normcoef[0][3]=1.145;
normcoef[0][4]=1.125; normcoef[0][5]=1.136;
normcoef[0][6]=1.148; normcoef[0][7]=1.145;
normcoef[0][8]=1.145; normcoef[0][9]=1.142;
normcoef[0][10]=1.148; normcoef[0][11]=1.125;
normcoef[0][12]=1.069; normcoef[0][13]=1.069;
normcoef[0][14]=1.082; normcoef[0][15]=0.0;
normcoef[1][0]=1.112; normcoef[1][1]=1.082;
normcoef[1][2]=1.044; normcoef[1][3]=1.056;
normcoef[1][4]=1.064; normcoef[1][5]=1.049;
normcoef[1][6]=1.484; normcoef[1][7]=1.464;
normcoef[1][8]=1.550; normcoef[1][9]=1.423;
normcoef[1][10]=1.560; normcoef[1][11]=1.518;
normcoef[1][12]=1.423; normcoef[1][13]=1.493;
normcoef[1][14]=1.469; normcoef[1][15]=1.498;

ifp = open(argv[1],O_RDONLY);

```

```

read(ifp, (char *)&day, sizeof(int));
read(ifp, (char *)&month, sizeof(int));
read(ifp, (char *)&year, sizeof(int));
read(ifp, (char *)&name, 32);
read(ifp, (char *)&max_mod, sizeof(int));

if (tty==2) {
    printf("Date: %d.", day);
    printf("%d.", month);
    printf("%d\n", year);
    printf("Setup_File name:%s\n", name);
    printf("Number of modules used:%d\n", max_mod);
}
for (i=0; i< max_mod; i++)
{
    read(ifp, (char *)&n[i], sizeof(int));
    read(ifp, (char *)&chnum[i], sizeof(int));

    if (tty==2) {
printf("Mod_%d :", n[i]);
printf("\nMax # of Channel used: %d\n", chnum[i]);
    }
    for (j=0; j< chnum[i]; j++) {
read(ifp, (char *)&ch_a[j][i], sizeof(int));

if (tty==2) {
    printf("Channels:ch%d ", ch_a[j][i]);
    printf("\n");
}
    }
    read(ifp, (char *)&N, sizeof(int));
    if (tty>0) {
        printf("Number of Events:%d\n", N);
        printf("Evt Mod ch0 ch1 ch2 ch3 ch4 ch5 ch6 ch7 ch8 ch9 ch10 ch11\n");
    }

    /* here start the loop do for all reading events */
    for(i=0; i<N; i++)
    {
if (tty>0) printf("-----\n");

        read(ifp, (char *)&no, sizeof(int));
        if (tty>0) printf("%4d", no);

        curr_channel=0;
        /* here starts the loop over the camac modules */
        for (curmod=0; curmod<max_mod; curmod++)
        {
            if ((curmod > 0) && (tty>0)) printf(" ");
            read(ifp, (char *)&cur_mod, sizeof(int));

            if (tty>0) {
                printf("%8d", cur_mod);
                printf(" ");
            }

            size =size2= 0;
            for(j=0; j<chnum[cur_mod] ;j++)
            {
                /* here i start filling the data arrays */
                read(ifp, (char *)&a, sizeof(int));
                read(ifp, (char *)&dummy, sizeof(int));
            }
        }
    }
}

```

```

        if (curr_channel <=15){
/* data is multiplied by a normalization coefficient for each ADC channel
   after the previously found 3.0 pedestal values subtraction */
data[0][curr_channel]=normcoef[0][curr_channel]*((float)dummy - 3.0);
        } else {
                data[1][curr_channel-16]=normcoef[1][curr_channel-16]
                        *((float)dummy -3.0); }

        curr_channel++;

        if (tty>0) {
size = (a-j)* 5 -size2;
if (size2 == 0) size2=size;
for (k = 0 ; k < size ;k++)
        printf(" ");
printf("%5d",dummy);
        }
        } /* end of loop over channels */
if (tty>0) printf("\n");
} /* end of loop over modules */

        /* here we start on searching valid data */
        ldat[0]=ldat[1]=0;

        for(ii=0; ii<2; ii++)
for (j=0; j<=15; j++) {
        if ((data[ii][j]<= maxdat) && (data[ii][j]>=mindat)) ldat[ii]=1;
        if (data[ii][j] > maxdat) {ldat[ii] = -1;break;}
}

        if ((ldat[0]==1) && (ldat[1]==1)) {
/* printf("data is valid: %d \n",i); */
/* since the data is valid ,now we start cluster analysis */
/* cluster length, cluster size and # of clusters */
/* one should eliminate multiple clusters */
clus_len[0]=clus_len[1] = 0;
clus_start[0]=clus_start[1] =0;
clus_num[0]=clus_num[1]=0;

for(jj=0; jj<=1; jj++) {
        for (ii=0; ii<=15; ii++) {

                if ( data[jj][ii] > clus_min ) {
/* aha, we are in a cluster */

                        if (clus_len[jj]==0) clus_start[jj]=ii;
/* thus we marked the beginning of a cluster */

                                clus_len[jj]++;
#ifdef DEBUG
                                printf("%f\n",data[jj][ii]);
#endif
                }
                if ((data[jj][ii] <= clus_min) && (clus_len[jj] >0)) {

                        /* the end of a cluster */
                        /* we keep clusters when only length is < 2 */
                        if ((clus_len[jj] < 2) || (clus_len[jj] > 6)){
                                clus_len[jj] = 0;
                                clus_num[jj] = 0;
                                clus_start[jj] =0;
#ifdef DEBUG
                                printf("rejecting... %d\n",clus_num[jj]);
#endif

```

```

    }
    else {
if(data[jj][ii-1]> clus_min) {
    clus_num[jj]++;
    tmp=(float)clus_len[jj];
    if ((tmp >=2.) && (tmp < 7.) ) {
        if (jj) hf1_(&h_cl_len_y, &tmp,&weight);
        else hf1_(&h_cl_len_x, &tmp,&weight);
    }
}
break;
    }
}

} /* end of loop over channels, ii */
} /*end of loop over x  and  y, jj */

tmp=(float)clus_num[0];
hf1_(&h_cl_mult_x,&tmp,&weight);
tmp=(float)clus_num[1];
hf1_(&h_cl_mult_y,&tmp,&weight);

if((clus_num[0] == 1) && (clus_num[1] == 1)) {
    /* aha! we have found a single cluster event... */

    ph_sum[0]=ch_sum[1]=ph_sum[1]=ch_sum[0]=0.;
    cog[0]=cog[1]=b[0]=b[1]=0.;
#ifdef DEBUG
    printf("x: %d,%d   y: %d\n",clus_len[0],clus_num[0],clus_len[1]);
#endif
    for (ii=0; ii<=1;ii++) {

        for(jj=clus_start[ii];jj<(clus_start[ii]+clus_len[ii]);jj++)
        {
ph_sum[ii]+=data[ii][jj];
/* original version where b is for all clusters */
/* b[ii]+=data[ii][jj]*ka; */
        ch_sum[ii]+=data[ii][jj]*((float) jj);

if(data[ii][jj]<0.) printf("warning! ,%d,%d,%f,%d\n"
                        ,ii,jj,data[ii][jj],clus_len[ii]);
ph_ave_sum[ii][jj]+=data[ii][jj];

if(ii == 0) hf1_(&h_ph_x,&data[ii][jj],&weight);
else hf1_(&h_ph_y,&data[ii][jj],&weight);

        }

        for(mm=0;mm<16;mm++) temp[mm]=data[ii][mm];
        ngu=15;
        cl_max_pos = maxrze_(temp,&ngu) - 1;
        dump[ii]=cl_max_pos;

#ifdef DEBUG
        printf("max is at %d\n",cl_max_pos);
#endif
        if((cl_max_pos>clus_start[ii])&&
            (cl_max_pos<(clus_start[ii]+clus_len[ii]-1))) {
            /* for restriction of calc of b to 3 channels */
            /* this feature is not used
for (mm=0;mm<=2; mm++){
b[ii]+=data[ii][cl_max_pos+mm-1]*ka;
}

```

```

    */
    for (mm=-1;mm<2; mm++)
    {
        ce[ii][mm+1]=data[ii][cl_max_pos+mm]-b[ii];
    }

    if((ce[ii][0]>0.) && (ce[ii][1]>0.) && (ce[ii][2]>0.)) {
cog[ii] = (ce[ii][0]*(cl_max_pos-1) + ce[ii][1]*(cl_max_pos) +
ce[ii][2]*(cl_max_pos+1)) / (ce[ii][0] + ce[ii][1] +
ce[ii][2]);

if ((ii==1) && (cog[0]!=0.) && (cog[1]!=0.)) {

    for (mm=0;mm<3; mm++)
    {
        sum_n[0][mm]+=ce[0][mm];
        sum_n[1][mm]+=ce[1][mm];
        sum_n2[0][mm]+=ce[0][mm]*ce[0][mm];
        sum_n2[1][mm]+=ce[1][mm]*ce[1][mm];
    }

    cog_count++;
    hf1_(&h_cog_x,&cog[0],&weight);
    hf1_(&h_cog_y,&cog[1],&weight);
    hf2_(&h_cogx_vs_cogy,&cog[0],&cog[1],&weight);}

    }
    else {
#ifdef DEBUG
printf("no cog calculated\n");
#endif
    }
    /* cog[ii]=(ch_sum[ii]/ ph_sum[ii]); */
}
}
#ifdef DEBUG
printf("clus len= %d for X cog= %f\n ",clus_len[0],cog[0]);
printf("clus len= %d for Y cog= %f\n ",clus_len[1],cog[1]);
#endif
valid++ ;

} /* end of single cluster event, endif */

} /* end of data matching min and max criteria, endif*/

} /* end of loop over events ,i */

printf("valid event no: %d for %s\n", valid,argv[1]);
/* calculate average pulse heights for each channel in cluster */

for(ii=0; ii<=1; ii++) {
    for(jj=0; jj<=15; jj++){

ph_ave[ii][jj]=ph_ave_sum[ii][jj] / valid ;
/*printf("average ph for %d , %d : %f\n",ii,jj,ph_ave[ii][jj]);*/
    }
}
for(mm=0;mm<2;mm++)
    for(ii=0; ii<=2; ii++) {
        cog_ave[mm][ii]=sum_n[mm][ii]/cog_count;
        cog_stdev[mm][ii] = sqrt(abs((sum_n2[mm][ii]*cog_count) -

```



```
(sum_n[mm][ii]*sum_n[mm][ii]))/cog_count;
    printf("wire=%d, ave=%f, stdev=%f\n", (dump[mm]+ii-1),
           cog_ave[mm][ii], cog_stdev[mm][ii]);
}
printf("cog count=%f\n", cog_count);
close(ifp);
hrput_(&izero, argv[3], "N", (long)strlen(argv[3]), 1L);
}
```

2. DATA Acquisition Program

```

/*****
 *  daq.c  version 1.0
 *
 *  GENERAL PURPOSE CAMAC DATA ACQUISITION PROGRAM
 *****/
 *
 *  written for gluon by Taylan Akdogan & NGU      02-03/1/97
 *****/
 *  MODIFICATIONS                                BY      DATE
 *  set a_max-=1 for lam operation(start @ 0!)    NGU    20/3/97
 *  write raw data as binary to disk              OC/NGU  13/10/97
 *  calculate data averages/write ascii to disc   MK/NGU  28/10/97
 *  Dont add 1&0 as data to histograms(1.0)      NGU    13/11/97
 *****/

#include <stdio.h>
#include <ib.h>
#include <sys/types.h>
#include <sys/stat.h>
#include <fcntl.h>
#include <string.h>
#include <math.h>
#include "f2c.h"
#include "daq.h"
#include "zaman.h"

extern int camWriteRead(int , ... );

#define MAXMOD 32
#define VERSION "1.0.1"

struct{
    float a[2000000];
}pawc_;
#define pawc_1 pawc_

extern int ibsta,ibcnt,iberr;

main(int argc,char **argv)
{
    extern int hrput_(),hbook1_(),hf1_(),hlimit_();
    char   cam_set[2],cam_resp[2];
    int    cam_x_status;
    int    dev0,dev_cam;
    int    f;
    int    i,ij,j,numread,dummy,N,Ncurrent=0,lam_cnt;
    /* N data to collect, Ncurrent current data */
    int    hlim=500000,hist_id=20,chtot=2048,izero=0; /* necessary stuff */
    float  chmin=0,chmax=2049,fzero=0,weight=1,data; /* for hbooking */
    unsigned char str[256];
    FILE    *fd,*fw,*file_mean;
    int     cur_mod;
    char histname[1024],histfilename[1024],rawfilename[1024];
    int a;

```

```

/* config file'dan okunacak degiskenler */
int   tty,do_hbook,max_mod,n[MAXMOD],num_bits[MAXMOD],hist_ch_num[MAXMOD];
int   a_max[MAXMOD],mask[MAXMOD],chnum[MAXMOD],ch_a[128][MAXMOD];
int   do_file,module_type[MAXMOD];
char  sttmp[32];

/*   date bilgileri */
int day=0 ,month=0 ,year =0 ;
/* a max of 64 subchannels to a max of MAXMOD modules */
int meandata[64][MAXMOD];

for (i=0;i<64;i++) for (j=0;j<MAXMOD;j++) meandata[i][j]=0;

fd=fopen(argv[1],"r");

fscanf(fd,"%d\n%d\n%d\n%s\n%d\n%s\n%d\n",
        &N,&tty,&do_hbook,histfilename,&do_file,rawfilename,&max_mod);
printf ("GENERAL DAQ PROGRAM, BOUNHEP Labs Version %s\n",VERSION);
printf("Number of Events=%d\ntty=%d\ndo_hbook=%d\nhistfilename=%s\n
        do_file=%d\nrawfilename=%s\nnumberof module=%d\n",
N,tty,do_hbook,histfilename,do_file,rawfilename,max_mod);
for (i=0;i<max_mod;i++) {
    fscanf(fd,"%d %d %d %d %d %d %d ",n+i,num_bits+i,mask+i,
            hist_ch_num+i,module_type+i,a_max+i,chnum+i);
    printf("module=%d #bit=%d mask=%d a_max=%d module_type=%d chnum=%d
channels: ", n[i],num_bits[i],mask[i],a_max[i],module_type[i],chnum[i]);
    for (j=0;j<chnum[i];j++)
        {fscanf(fd,"%d",&(ch_a[j][i]));printf("%d ",ch_a[j][i]);}
    fscanf(fd,"\n");
    printf("\n");
}
fclose(fd);

/*  N=  NUMBER of READINGS
    tty=  Do we want reporting?
    do_hbook=  Do we want histo package?
    do_file= Do we want to store raw data?
    max_mod=  Number of modules
    n[]=  the array which contains the slot numbers
    num_bits[]=  the resolution of each module
    mask[]= mask for the last byte
    hist_ch_num[]= Channel number for histogram for each module
    a_max[]=  array which contains the max channel for each module type
    chnum[]=  the array to give the max number of channels to read
    ch_a[][]= channellist, module number
    module_type = adc tdc what?      */
date(&day,&month,&year);
/*opens the file to store row data
    last parameter is for file permissions*/
fw = open(rawfilename,O_CREAT|O_WRONLY,0644);
write(fw,(char *)&day,sizeof(int));
write(fw,(char *)&month,sizeof(int));
write(fw,(char *)&year,sizeof(int));
strncpy(sttmp,argv[1],32);
write(fw,sttmp,32);

```

```

write(fw,(char *)&max_mod,sizeof(int));
for (i=0;i< max_mod; i++) {
    write(fw,(char *)&n[i],sizeof(int));
    write(fw,(char *)&chnum[i],sizeof(int));
    for (j=0;j<chnum[i];j++) {
        write(fw,(char *)&ch_a[j][i],sizeof(int));
    }
}
write(fw,(char *)&N,sizeof(int));

/* to test if the GPIB and CAMAC are up & running */
if((dev0 = ibfind("gpib0")) & ERR) {gpiberr("ibfind err"); exit(1); }
printf("The Interface board is OK.\n");
if( ibsic(dev0) & ERR ) {gpiberr("ibsic Err"); exit(1); }
printf("InterFace board Cleared.\n");
if((dev_cam = ibfind("camac")) & ERR){gpiberr("ibfind err"); exit(1); }
printf("The Camac is OK.\n");

/* hbooking stuff is done if the switch is set */
if (do_hbook) {
    hlimit_(&hlim);
    printf("Booking for hist_ID(s) : ");
    for (i=0;i<max_mod;i++) for (j=0;j<chnum[i];j++) {
        hist_id=n[i]*1000+ch_a[j][i];
        printf (" %d ",hist_id);
        sprintf(histname,"M%d-Ch%d",n[i],ch_a[j][i]);
        chtot=hist_ch_num[i];
        chmin=0.0;
        chmax=pow(2,num_bits[i]);
        hbook1_(&hist_id,histname,&chtot,&chmin,&chmax,&fzero,11L);
    }
}
printf("\n");

/* Send to crate initialization signal (Z) */
if (camWriteRead(dev_cam,0,2,str,1,33)==-1) exit(-1);
/* Send to crate common clear signal (C) */
if (camWriteRead(dev_cam,0,2,str,1,34)==-1) exit(-1);
/* Start 16 bit data transfer */
if (camWriteRead(dev_cam,0,2,str,1,98)==-1) exit(-1);

for (cur_mod=0;cur_mod<max_mod;cur_mod++) {
    /* clear LAM */
    if (camWriteRead(dev_cam,0,2,str,3,CLEAR_LAM,(a_max[cur_mod]-1),
        n[cur_mod])===-1) exit(-1);
    /* enable LAM */
    if (camWriteRead(dev_cam,0,2,str,3,LAM_ENABLE,(a_max[cur_mod]-1),
        n[cur_mod])===-1) exit(-1);
    printf("\n");
}

/* here start the loop, do for all events */
for(i=0;i<N;i++)
{
    if (do_file) { write(fw,(char *)&i,sizeof(int));}
}

```

```

        for (cur_mod=0;cur_mod<max_mod;cur_mod++) {
/* clear LAM */
camWriteRead(dev_cam,0,2,str,1,98);
if (camWriteRead(dev_cam,0,2,str,3,CLEAR_LAM,(a_max[cur_mod]-1),
                n[cur_mod])===-1)        exit(-1);
/* enable LAM */
camWriteRead(dev_cam,0,2,str,1,98);
if (camWriteRead(dev_cam,0,2,str,3,LAM_ENABLE,(a_max[cur_mod]-1),
                n[cur_mod])===-1)        exit(-1);
        }

/* here start the loop over the camac modules */
for (cur_mod=0;cur_mod<max_mod;cur_mod++) {

/*
this is to test the lam
dummy=lam_cnt=0;
while (dummy!=3) {
camWriteRead(dev_cam,2,4,str,3,8,(a_max[cur_mod]-1),n[cur_mod]);
dummy=(int)str[2]; lam_cnt++;
#ifdef DEBUG
printf("rsp=%d    mod=%d  ch=%d\n ",(int)str[2],cur_mod, a);
#endif
if (lam_cnt==7) break;
}
*/

        if (do_file) { write(fw,(char *)&cur_mod,sizeof(int)); }

if (tty) printf("slot=%2d  %5d.cnts ->",n[cur_mod],i);
/* loop over channels */
for(j=0; j<chnum[cur_mod] ;j++)
{

a=ch_a[j][cur_mod];
if (do_file) {write(fw,(char *)&a,sizeof(int));}

camWriteRead(dev_cam,0,2,str,1,98);
data=(float)dummy=
    camWriteRead(dev_cam,mask[cur_mod],4,str,3,READ_FUNCT,a,n[cur_mod]);
meandata[j][cur_mod]+=data;

if (tty) printf("%5d",dummy);
/*    if (data > 1.0) { Ncurrent+=1;} */
if (do_hbook && (data>1.0))    { hist_id=(1000*n[cur_mod] +a);
hf1_(&hist_id,&data,&weight);
}
if (do_file) {write(fw,(char *)&dummy,sizeof(int));}
} /* end of loop over channels */
if (tty) printf("\n");
    } /* end of loop over camac modules */

/*    if (Ncurrent >= N) {break;} */
} /* end of loop for reading events */

```

```

/* put data to HBOOK */
if (do_hbook) hrput_(&izero,histfilename,"N",(long)strlen(histfilename),1L);
printf("Finished.\n");
close(fw);

/* put the average in each channel to a file */
file_mean=fopen("averages","w");

for (cur_mod=0;cur_mod<max_mod;cur_mod++)
  for(j=0; j<chnum[cur_mod] ;j++)
    { printf(" ave of module %d   channel %d is %f\n",
      cur_mod,ch_a[j][cur_mod],(float)meandata[j][cur_mod]/(float)N);
      fprintf(file_mean,"%f\n", (float)meandata[j][cur_mod]/(float)N);
    }
  fclose(file_mean);
}
/* end of main */

gpiberr(char *msg) {

  printf("%s\n",msg);
  printf("ibsta=0x%x  <",ibsta);

  if ( ibsta & ERR ) printf(" ERR");
  if ( ibsta & TIMO ) printf(" TIMO");
  if ( ibsta & END ) printf(" END");
  if ( ibsta & SRQI ) printf(" SRQI");
  if ( ibsta & RQS ) printf(" RQS");
  if ( ibsta & CMPL ) printf(" CMPL");
  if ( ibsta & CIC ) printf(" CIC");
  if ( ibsta & ATN ) printf(" ATM");
  if ( ibsta & TACS ) printf(" TACS");
  if ( ibsta & LACS ) printf(" LACS");

  printf(" >\n");

  printf("iberr= %d", iberr);
  if ( iberr == EDVR ) printf(" EDVR <OS Error>\n");
  if ( iberr == ECIC ) printf(" ECIC <Not CIC>\n");
  if ( iberr == ENOL ) printf(" ENOL <No Listener>\n");
  if ( iberr == EADR ) printf(" EADR <Adress Error>\n");
  if ( iberr == EARG ) printf(" ECIC <Invalid Argument>\n");
  if ( iberr == ESAC ) printf(" ESAC <No Sys Ctrlr>\n");
  if ( iberr == EABO ) printf(" EABO <Operation Aborted>\n");
  if ( iberr == ENEB ) printf(" ENEB <No Gpib Board>\n");
  if ( iberr == EOIP ) printf(" EOIP <Async I/O in prg>\n");
  if ( iberr == ECAP ) printf(" ECAP <No Capability>\n");
  if ( iberr == EFSO ) printf(" EFSO <File sys. error>\n");
  if ( iberr == EBUS ) printf(" EBUS <Command error>\n");
  if ( iberr == ESTB ) printf(" ESTB <Status byte lost>\n");
  if ( iberr == ESRQ ) printf(" ESRQ <SRQ stuck on>\n");
  if ( iberr == ETAB ) printf(" ETAB <Table Overflow>\n");
  if ( iberr == EPAR ) printf(" EPAR <Parse Error in Config>\n");
  if ( iberr == ECFG ) printf(" ECFG <Can't open Config>\n");
  if ( iberr == ETAB ) printf(" ETAB <Device Table Overflow>\n");
  if ( iberr == ENSD ) printf(" ENSD <Configuration Error>\n");

```

```
printf("ibcnt= %d\n", ibcnt );  
printf("\n");  
}
```

3. PMT Scan Program

```

/* *****
 * PMT surface scanning program, written by Muge Karagoz *
 * ***** */

#include <stdio.h>
#include <string.h>
#include <stdlib.h>
#include <unistd.h>

int main () {

    int ystepsize=38,xstepsize=640;
    int ycur=0, xcur=0;
    int ystepmax=684;
    /* int ystepmax=10240; */
    int xstepmax=6400;
    char outword[64], tmp[64];

    while ( ycur <= ystepmax) {

        system("genel gui/setup/readall.setup");
        sprintf(tmp,"cp readall.dat /mnt/xtalk/xtalk-%d-%d.dat",ycur,xcur);
        system(tmp);

        xcur+=xstepsize;

        if ( xcur > xstepmax) {
            /* A line is scanned, move the cursor back */
            ycur +=ystepsize;
            xcur=0;
            /* motor x i xstepmax */
            strcpy(outword,"motor x i ");
            sprintf(tmp,"%d",xstepmax);
            strcat(outword,tmp);
            system(outword);
            /* motor y g ystepsize */
            strcpy(outword,"motor y g ");
            sprintf(tmp,"%d",ystepsize);
            strcat(outword,tmp);
            system(outword);
            printf ("going in x backward %d steps\n", xstepmax);
            printf ("going in y forward %d steps\n", ystepsize);
            sleep (6);
        } else {
            printf("Going in x for %d steps\n",xstepsize );
            strcpy(outword,"motor x g ");
            sprintf(tmp,"%d",xstepsize);
            strcat(outword,tmp);
            system(outword);
            sleep (3); }
    }
    printf ("Bitttiii\n");
}

```


4. Image Reconstruction Program

```

C      *****
C      Image Reconstruction Program, Written by Muge Karagoz
C      *****
      program sinogram
      common/pawc/pawc(10000)
      dimension sino(50,4)
      dimension fback(50,50)
      call hlimit(10000)
      M=4
      PI=3.1415
      itot=50
      ground=0.
      call hbook2(1,'lego',50,0.,50.,50,0.,50.,0.0)
      open (17,'line0.sin')
      open (18,'line45.sin')
      open (19,'line90.sin')
      open (20,'line135.sin')
      do j= 1,itot
        read(17,*) sino(j,1)
        read(18,*) sino(j,2)
        read(19,*) sino(j,3)
        read(20,*) sino(j,4)
      enddo

      do j= 1,itot
        sino(j,2)=sino(j,2)*2.5
      enddo

      do ix=1,itot
        do iy=1,itot
          do j=0,M-1
            fback(ix,iy)=fback(ix,iy)+
C      & sino((ix*cos((PI/M)*j))+iy*sin((PI/M)*j),j+1)
            write (*,*) ix*cos((PI/M)*j)+iy*sin((PI/M)*j)
          enddo
        enddo
      enddo

      do ix=1,50
        write (*,10) (nint(fback(ix,iy)*255./2367.),iy=1,50)
      enddo

      do ix=1,itot
        do iy=1,itot
          signal=fback(ix,iy)
          call hf2(1,ix*1.-.5,iy*1.-.5,signal)
        enddo
      enddo

20     FORMAT (20(1X,F6.1))
10     format (20(1x,i3))
      call hrput(0,'legox.hst','n')
      stop
      end

```

References

- [1] Atac, M., "Medical Imaging and Particle Astrophysics," in *Instrumentations in Elementary Particle physics, Proceedings of the VII ICFA School*, Leon-Mexico, July 1997, pp. 191-207, AIP, New York, 1998.
- [2] Shung, K. K., Smith, M. B., Tsui, B. M. W., *Principles of Medical Imaging*, Academic Press, California, 1992.
- [3] Anger, H. O., "Tomography and Other Depth-Discrimination Techniques," in *Instrumentation in Nuclear Medicine*, G. J. Hine and J. A. Sorenson (Eds.), pp. 61-100, Vol. 2, Academic Press, New York and London, 1974.
- [4] Anger, H. O., "Radioisotope Cameras," in *Instrumentation in Nuclear Medicine*, G. J. Hine and J. A. Sorenson (Eds.), pp. 487-552, Vol. 2, Academic Press, New York and London, 1974.
- [5] Townsend, D. W., "Medical Imaging," CERN Summer School Lectures, Geneva, 1996.
- [6] Rogers, J. G., Taylor, A. J., et al., "An Improved Multicrystal 2-D BGO Detector for PET," *IEEE Tra. on NS.*, Vol. 39, No. 4, 1063-1068, 1992.
- [7] Townsend, D. W., Byars, L.G., Defrise, M., et al., "Design and Performance of a Rotating Positron Tomograph, RPT-2", 1997, <http://www.pet.upmc.edu/pet4.txt>
- [8] Moses, W. W., Virador, P. R. G., Derenzo, S. E., et al., "Design of a High-resolution, High Sensitivity PET Camera for Human Brains and Small Animals," *IEEE Tra. on NS.*, Vol. 44, No. 4, pp. 1487-1491, 1997.

- [9] Moses, W. W., Derenzo, S. E., et al., "A Room Temperature LSO/PIN PD PET Detector Module that Measures DOI," *IEEE Tra. on NS.*, Vol. 42, pp. 1085-1089, 1995.
- [10] Schmelz, C., Bradbury, S. M., et al., "Feasibility Study of an Avalanche Photodiode readout for a High Resolution PET with nsec Time Resolution," *IEEE Trans. on Nuclear Science*, Vol. 42., No. 4., 1995.
- [11] Moisan, C., Rogers, J. G., et al., "Design Studies of a Depth Encoding Large Aperture PET Camera," *Proceedings of the Nuclear Science Symposium Medical Imaging Conference*, Norfolk, 30 October-5 November 1994.
- [12] Townsend, D. W., Defrise, M., "Image Reconstruction Methods in Positron Tomography", CERN Yellow Reports 93-02, Geneva, 1993.
- [13] Cherry, S. R., Dahlbom, M., et al., "3D PET Using a Conventional Multislice Tomograph without Septa," *J. Comput. Assist. Tomogr.*, Vol. 15, pp. 655-668, 1991.
- [14] Ziegler, S. I., Ostertag, H., et al., "Effects of Scintillation Light Collection on the Time Resolution of a Time-of-Flight Detector for Annihilation Quanta," *IEEE Trans. on NS.*, Vol. 37, No. 2, 1990
- [15] Birks, J. B., *The Theory and Practice of Scintillation Counting*, Pergamon Press, 1964.
- [16] Leo, W. R., *Techniques for Nuclear and Particle Physics Experiments*, Springer-Verlag, Berlin, 1992.
- [17] Knoll, G. F., *Radiation Detection and Measurement*, 2nd Ed., John Wiley & Sons, 1989.
- [18] Bock, R. K., *The Particle Detector Briefbook*, November 1998,
<http://www.cern.ch/Physics/ParticleDetector/Briefbook>
- [19] Heitler, W., *The quantum theory of radiation*, 3rd ed., Oxford:Clarendon press, 1953

- [20] Fernow, R., *Introduction to Experimental Particle Physics*, Cambridge University Press, 1992
- [21] Singru, R. M., *Introduction to Experimental Nuclear Physics*, John Wiley and Sons, New York, 1974
- [22] Davisson, C. M., *Alpha-, Beta- and Gamma-Ray Spectroscopy*, Ch. 2, Ed. Siegbahn, K., North-Holland Publ. Co., Amsterdam, 1965
- [23] Klein, O., Nishina, Y., *Z. Physik*, Vol.52, pp. 823-??, 1929
- [24] Delaney, C. F. G., Finch, E. C., *Radiation Detectors*, Clarendon Press, Oxford, 1992.
- [25] Kubota, S., Murakami, H., "The New Scintillation Material CsI and its Application to Position Sensitive Detectors", *NIM in Physics Research* A273, 645-649, 1988.
- [26] Majewski, S., Zorn, C., *Fast Scintillators for High Radiation Levels*, Vol. 9, Part 1, *Instrumentation in High Energy Physics*, Advanced Series on Directions in High Energy Physics, World Scientific, Singapore, 1992.
- [27] Kubota, S., Sakuragi, S., et al, "A New Scintillation Material: Pure CsI with 10 ns Decay Time", *NIM in Physics Research* A268, 275-277, 1988.
- [28] Bicron Company, "Inorganic Products", 1997, <http://www.bicron.com/CSI.htm> .
- [29] Bicron Company, "Inorganic and Organic Scintillators Differences and Similarities", 1998, <http://www.bicron.com/> .
- [30] Derenzo, S. E., Moses, W. W., et al., "Critical Instrumentation Issues for < 2 mm Resolution, High Sensitivity Brain PET," in *Quantification of Brain Function*, pp. 25-37, Elsevier Science Publishers, Amsterdam, 1993.
- [31] Del Guerro, L., "Detector Applications in Medicine and Biology," CERN Summer School Lectures, Geneva, 1995
- [32] Moses, W. W., and Derenzo, S. E., "Scintillators for Positron Emission Tomography", presented at SCINT '95, Delft, 1995.

- [33] GEANT - Detector Description and Simulation Tool, CERN Program Library Long Writeup, Geneva, 1995.
- [34] CERNLIB - CERN Program Library, CERN Program Library Short Writeups, Geneva, 1995.
- [35] ZEBRA - Reference Manual, CERN Program Library Long Writeups, Geneva, 1995.
- [36] HBOOK - Reference Manual, CERN Program Library Long Writeups, Geneva, 1995.
- [37] PAW - Physics Analysis Workstation: An Introductory Tutorial, CERN Program Library Long Writeups, Geneva, 1995.
- [38] Bird, A. J., et al., "Multi-channel Readout of Crossed-wire Anode Photomultipliers", NIM in Physics Research A 348, pp. 668-672, 1994.
- [39] Hamamatsu Corporation, Private Communication, 1997.
- [40] Husain, K., et al., *Linux Unleashed*, 2nd Ed., SAMS Publishing Co., 1996.
- [41] Schroeter, C., Linux-GPIB User's Guide, unpublished, 1994
- [42] Boun HEP Group, "Photoelectron Counting Using a Position Sensitive Photomultiplier under Linux", Balkan Physics Letters, Vol. 5, No 3, pp 179-187, 1997.
- [43] Millman, J., Halkias, C., *Integrated Electronics: Analog and Digital Circuits and Systems*, McGraw-Hill, Singapore, 1971.
- [44] Koroglu, A., "Scintillating Fiber Detectors", MS. Thesis, Boğaziçi University, 1997.
- [45] Particle Data Group, "Review of Particle Physics", Phys. Rev. D, Vol. 54, No. 1, 1996.
- [46] EG&G ORTEC, Catalog of Instruments and Systems for Nuclear Spectroscopy, TN, 1993.

- [47] Bassini, R., et al., "A Fully Programmable 16 Channel Spectroscopy Amplifier in a Single NIM Unit," IEEE Trans. on Nuclear Science, Vol. 42, No. 4, pp. 719-723, 1995.
- [48] Moranesi, P., et al., L'Amplificatore Operazionale, Ed. Boringhieri, 1978.
- [49] Zirkle, R.E., "Biological Effectiveness of Alpha Particles as a Function of Ion Concentration Produced in Their Paths," Am. J. Cancer, Vol. 23, pp. 558-567, 1935.
- [50] Wilson, R. R., "Radiological Use of Fast Protons", Radiology, Vol. 47, No. 5, pp. 487-491, 1946 .
- [51] Optivus Technology, Inc., 1998, <http://www.optivus.com/bragg.html>.
- [52] Snyder, W. S., et al., "Report of the Task Group on Reference Man," Publication No. 23, ICRP, 1974.